scientific reports

Check for updates

OPEN

# Revisiting the Rytov approximation in diffuse optics and its applications for the inverse and forward problems

Angelo Sassaroli[1]✉, Giles Blaney[1], Fabrizio Martelli[2] & Sergio Fantini[1]

**We propose an overview of the Rytov approximation in diffuse optics of biological tissues, for the inverse and forward problems. First, we show a physical interpretation of the Rytov approximation as a type of partial pathlength (named fluence rate partial pathlength) which is distinct from the usual partial pathlength for reflectance measurements. Second, we study the accuracy of the Rytov approximation for the calculation of Jacobians considering absorption perturbations and reflectance measurements. For higher absorption and lower reduced scattering values the discrepancy between the true Jacobian (i.e., the reflectance partial pathlength) and that obtained with the Rytov approximation (i.e., the fluence rate partial pathlength) can be up to about 70% for diffusion theory calculations and up to about 25% for Monte Carlo simulations. For higher reduced scattering values, the discrepancies become less than 10%. Third, we propose a calibration method that can circumvent numerical inaccuracies when the calculation of Jacobians is carried out in presence of highly absorbing layers. Finally, fourth, we also propose an original formula derived from the Rytov approximation for reflectance measurements, and we show how it performs for the forward problem, when we consider defects with large absorption contrast with respect to the background.**

**Keywords** Rytov approximation, Monte Carlo, Diffusion equation, Adjoint method, Reciprocity theorem

There is a vast amount of literature about the Born or Rytov approximation/series for solving the Helmholtz equation that arises in many fields of research. Applications include studies of weakly scattering media[1–3], seismic waveforms in geophysics[4,5], and optics in highly scattering media[6,7]. In this work, we focus on the latter, particularly on diffuse optics of biological tissues, where these two approximations have been applied for linearizing the integral equations obtained for solving the diffusion equation (DE) (the DE can always be reduced to a Helmholtz equation by a change of variables[6]). These integral equations link the source of perturbation (e.g., a change in the optical properties) to the change in fluence rate inside the medium or the change in exiting flux (or reflectance) measured by an optical detector on the surface of the medium. A linearization of these equations allows for a straightforward inversion of the integral equations for recovering the change in the optical properties. This is a fundamental step also for nonlinear methods of spatial reconstruction. Two major applications in diffuse optics of biological tissues are near infrared spectroscopy (NIRS) [or diffuse optical tomography (DOT)][6,8,9] and fluorescence imaging[10,11]. The advantages of the Rytov over the Born approximation have been discussed in several works[6,8,9]. They can be associated with the fact that while the Born approximation is linear in the change of the optical properties, the Rytov approximation contains higher powers of these changes, and for this reason it can describe some nonlinear effects.

More recently, with the advent of graphic processing units (GPU), Monte Carlo (MC) simulations have become increasingly important for simulating light propagation in tissues[12–14]. MC simulations allow for solving the radiative transfer equation (RTE)[15] for any geometry and spatial distribution of the optical properties without approximations. Due to the increased speed in computation of GPU, MC simulations can be efficiently used as a forward problem solver embedded in inversion procedures[16]. Also, MC simulations allow for the fast computation of sensitivity functions (i.e., Jacobians) under general conditions of validity of the RTE[16]. In this regard, a coupled forward-adjoint method has been proposed for improving the variance of the sensitivity functions obtained with conventional methods[17,18]. For the case of sensitivity to absorption changes, the

[1]Department of Biomedical Engineering, Tufts University, 4 Colby Street, Medford, MA 02155, USA. [2]Dipartimento di Fisica e Astronomia, Università degli Studi di Firenze, Via G. Sansone 1, 50019 Sesto Fiorentino, Florence, Italy. ✉email: angelo.sassaroli@tufts.edu

conventional methods consist of mean pathlength calculations based on the intersection of detected photon trajectories with a region of interest (for which the Jacobian is calculated). In fact, for media verifying the microscopic Beer–Lambert law, the Jacobian of both the fluence rate and the reflectance with respect to the absorption coefficient of a region of interest have the physical meaning of mean pathlength of "detected photons" in the region of interest (see for example Eq. (11) in section "A random multivariate approach to perturbation theory of photon transport"). The coupled forward-adjoint method is rigorous and can be used in total generality within the validity of the RTE. However, due to the prohibitive memory requirement for typical problems in NIRS and DOT, the method has been used only for applications where one considers relatively short source-detector separations (less than about 5 mm) where small tissue volumes are probed (e.g., skin)[17]. For NIRS-DOT applications, whenever diffusion conditions are satisfied, a coupled forward-adjoint method based on the Rytov approximation has been proposed for the computation of Jacobians with Monte Carlo simulations[19,20]. If the measurement of interest is the fluence rate at a field point ($\mathbf{r}$) due to a source point at $\mathbf{r}_0$, under the Rytov approximation, the continuous wave (CW) Jacobian for localized absorption perturbations with volume $dV$ at location $\mathbf{r}'$, is obtained from the computation of three Green's functions: (1) the Green's function of the fluence rate at $\mathbf{r}'$ due to a point source at $\mathbf{r}_0$, $G_{\phi_0}(\mathbf{r}_0 \rightarrow \mathbf{r}')$; (2) the Green's function of the fluence rate at the field point $\mathbf{r}$ due to a point source at $\mathbf{r}'$, $G_{\phi_0}(\mathbf{r}' \rightarrow \mathbf{r})$; (3) the Green's function of the fluence rate at the field point $\mathbf{r}$ due to a point source at $\mathbf{r}_0$, $G_{\phi_0}(\mathbf{r}_0 \rightarrow \mathbf{r})$. For fluence rate calculations, the use of the reciprocity relationship ($G_{\phi_0}(\mathbf{r}' \rightarrow \mathbf{r}) = G_{\phi_0}(\mathbf{r} \rightarrow \mathbf{r}')$) makes this approach particularly effective. In fact, the Jacobian at all voxels requires only two MC simulations: (1) the direct simulation defined by placing an isotropic point source at $\mathbf{r}_0$ to calculate $G_{\phi_0}(\mathbf{r}_0 \rightarrow \mathbf{r}')$ for all $\mathbf{r}'$; (2) an adjoint simulation obtained by placing a point source at $\mathbf{r}$ to calculate $G_{\phi_0}(\mathbf{r} \rightarrow \mathbf{r}')$ for all $\mathbf{r}'$. The Jacobian is obtained by $\frac{G_{\phi_0}(\mathbf{r}_0 \rightarrow \mathbf{r}')G_{\phi_0}(\mathbf{r} \rightarrow \mathbf{r}')}{G_{\phi_0}(\mathbf{r}_0 \rightarrow \mathbf{r})} dV$, where $dV$ is the volume of the absorption perturbation at $\mathbf{r}'$. In this case, the only hypothesis needed for using the Rytov approximation is that diffusion conditions are satisfied. However, we notice that by using MC-based Green's functions of the fluence rate, we are considering a hybrid method that can be effective for the calculation of Jacobians for a wide range of the baseline optical properties; most likely more effective than for the case when DE based Green's functions are used.

For the calculation of Jacobians for reflectance measurements, the last two steps of the Jacobian calculation for the fluence rate must be modified in the following way[21]: (2a) the reflectance per unit source power calculated at the detector ($\mathbf{r}_b$) due to a point source at the voxel $\mathbf{r}'$, $R_0(\mathbf{r}' \rightarrow \mathbf{r}_b)$; (3a) the reflectance per unit source power calculated at the detector due to a point source at $\mathbf{r}_0$, $R_0(\mathbf{r}_0 \rightarrow \mathbf{r}_b)$. In this case, the Jacobian is obtained as $\frac{G_{\phi_0}(\mathbf{r}_0 \rightarrow \mathbf{r}')R_0(\mathbf{r}' \rightarrow \mathbf{r}_b)}{R_0(\mathbf{r}_0 \rightarrow \mathbf{r}_b)} dV$. In step (2a) a generalized reciprocity relationship based on the properties of RTE[17,22] can be used to replace $R_0(\mathbf{r}' \rightarrow \mathbf{r}_b)$ with the calculation of the Green's function of the fluence rate at $\mathbf{r}'$ due to an adjoint source at $\mathbf{r}_b$ (i.e.,$G_{\phi_0}(\mathbf{r}_b \rightarrow \mathbf{r}')$), which is specified by the detector's position, size, and emittance angle (which must match the acceptance angle in the direct calculation; see section "Relationship between the correct forward-adjoint method and the present work")[17]. This calculation should also consider the refractive index mismatch between diffusive and outer medium. Again, this allows for the calculation of the Jacobian at all voxels with only two simulations. Adjoint method calculations for reflectance measurements are also known in diffusion theory (DT) by use of a Robin source[6]. Also, in most literature where the DE is used[23–26] the Jacobians for reflectance and fluence rate measurements are considered equivalent because of the adoption (not always openly disclosed) of the partial current boundary condition (PCBC)[6,15]: $R_0(\mathbf{r} \rightarrow \mathbf{r}_b) = \frac{G_{\phi_0}(\mathbf{r} \rightarrow \mathbf{r}_b)}{2A(n_r)}$, where $A(n_r)$ is a constant that depends on the local refractive index mismatch ($n_r$) between diffusive and outer medium at $\mathbf{r}_b$.

In this work, we investigate the calculation of Jacobians for absorbing perturbations, by showing several comparisons using both DT and MC simulations. MC simulations are used for both the calculation of fluence rate in the Rytov approximation, and for the calculation of the mean pathlengths for reflectance measurements (i.e., the correct Jacobians) in regions of interest. The main purpose of this work is to test, for a wide range of optical properties, the performance of the Rytov approximation for the calculation of Jacobians when the measurement of interest is the reflectance. A good part of our effort is dedicated to pointing out the physical meaning of the Rytov and Born approximations. This viewpoint provides a more intuitive picture on the photon transport process. For this purpose, we reframe the general perturbative approach to photon migration by using a definition of the fluence rate based on a random multivariate probability density function derived from the microscopic Beer–Lambert law (section "A random multivariate approach to perturbation theory of photon transport"). The concept of fluence rate partial pathlength moment is introduced and an explicit formula for a general moment is provided under diffusion conditions. The Born and Rytov approximations of the DE are introduced in section "Born and Rytov approximations and their physical meaning". It is immediately recognized how these expressions depend on the fluence rate partial pathlength ($\langle l_i \rangle_\phi$) in a region of interest. In section "Calculation of reflectance based on Born and Rytov approximations" we provide an original formula for the reflectance under the Rytov approximation. The difference between the fluence rate and the reflectance partial pathlengths ($\langle l_i \rangle_R$) are discussed more in detail. In section "Relationship between the correct forward-adjoint method and the present work" we briefly review the rigorous coupled forward-adjoint method[17] and we provide the links to the present work. In sections "Diffusion theory calculations" and "Monte Carlo simulations" the details of diffusion and MC calculations are provided, respectively. The results are described in section "Results". Section "Comparison of MC and diffusion theory results for the calculation of reflectance pathlengths" is dedicated to the comparison of reflectance partial pathlengths obtained independently with two MC codes and with DT. Section "Comparison of MCX and diffusion theory results for the calculation of fluence rate and reflectance pathlengths" is dedicated to the comparison of the Jacobians obtained with the Rytov approximation

for both DT and MC calculations. The reflectance partial pathlength obtained with MC (the true parameter of interest) is also shown for comparison. In section "Comparison of fluence rate pathlengths in presence of a highly absorbing thin layer" the same comparisons of section "Comparison of MCX and diffusion theory results for the calculation of fluence rate and reflectance pathlengths" are shown for a medium containing a highly absorbing thin layer. Section "Calculations of reflectance perturbation due to a strong localized absorption change" shows two examples of reflectance change for a wide range of absorption change that spans the linear and nonlinear regime. In this section we compare MC and DT calculations under the Born, Rytov and higher order (up to the fourth order) Born series. In section "Discussions" the results are discussed, and in section "Conclusions and future work" we summarize the main results in the conclusions.

## Theory

### A random multivariate approach to perturbation theory of photon transport

The physical basis of this section is the microscopic Beer–Lambert law[21,27,28] (mBLL) which allows for a random multivariate framework of photon transport in a medium with an arbitrary spatial distribution of the scattering and absorption coefficients. This is the approach used in Monte Carlo methods for solving the RTE[15]. Here we replicate the method used in our previous publication[21] but instead of focusing on the reflectance at a boundary point, we focus on the fluence rate at an arbitrary point inside a turbid medium. The theory is described for the continuous-wave domain (CW) but it can be developed also for time-domain and frequency-domain.

We divide a medium (of arbitrary non-concave geometry) into $N$ regions (of arbitrary shape) characterized by absorption and scattering coefficients $\mu_{ai}, \mu_{si} (i = 1,2, ..., N)$, respectively. When light is emitted by a point source at $\mathbf{r}_0$, the fluence rate at a point $\mathbf{r}$ can be defined by using a random multivariate probability density function (*pdf*) $f_0(l_1, l_2, \ldots, l_N)$ normalized such that:

$$G_{\phi_0}(\mathbf{r}_0 \to \mathbf{r}) = \int_{\mathbb{R}^{N+}} f_0(l_1, l_2, \ldots, l_N)\, dl_1 dl_2 \cdots dl_N \tag{1}$$

where $G_{\phi_0}$ is the Green's function of the fluence rate ($[G_{\phi_0}] = \mathrm{L}^{-2}$), and $f_0(l_1, l_2, \ldots, l_N)$ is the *pdf* ($[f_0] = \mathrm{L}^{-N-2}$) that a photon emitted at $\mathbf{r}_0$ and found at $\mathbf{r}$ spends the pathlengths $l_1, l_2, \ldots, l_N$ in the regions $1,2, ..., N$, respectively. Note that strictly speaking $f_0$ is not a *pdf*, since it is not normalized to "1". However, this fact is irrelevant for developing our arguments. For conciseness, in Eq. (1), we consider the dependence of $f_0$ on $\mathbf{r}_0$ and $\mathbf{r}$ as implicit. For an arbitrary perturbation of the absorption coefficient $\Delta\mu_{ai} (i = 1, ..., N)$, based on the microscopic Beer–Lambert law[27], the new *pdf* will be:

$$f_p(l_1, l_2, \ldots, l_N) = f_0(l_1, l_2, \ldots, l_N)\, e^{-\sum_{i=1}^{N} l_i \Delta\mu_{ai}} \tag{2}$$

The integration of $f_p$ in $\mathbb{R}^{N+}$ yields $G_{\phi_p}(\mathbf{r}_0 \to \mathbf{r})$, i.e., the Green's function of the perturbed fluence rate:

$$G_{\phi_p}(\mathbf{r}_0 \to \mathbf{r}) = \int_{\mathbb{R}^{N+}} f_p(l_1, l_2, \ldots, l_N)\, dl_1 dl_2 ... dl_N \tag{3}$$

By using a multivariate Taylor expansion of the exponential, we obtain:

$$G_{\phi_p}(\mathbf{r}_0 \to \mathbf{r}) = G_{\phi_0}(\mathbf{r}_0 \to \mathbf{r}) \sum_{k_1,k_2,\ldots,k_N=0}^{\infty} (-1)^{k_1+k_2+\ldots+k_N} \frac{\langle l_1^{k_1} l_2^{k_2} \ldots l_N^{k_N} \rangle_\phi}{k_1! k_2! \ldots k_N!} \Delta\mu_{a1}{}^{k_1} \Delta\mu_{a2}{}^{k_2} \ldots \Delta\mu_{aN}{}^{k_N} \tag{4}$$

where $\langle l_1^{k_1} l_2^{k_2} \ldots l_N^{k_N} \rangle_\phi$ is the mixed pathlength moment of order $k_1 + k_2 + \cdots + k_N$ defined by the relation:

$$\langle l_1^{k_1} l_2^{k_2} \ldots l_N^{k_N} \rangle_\phi = \frac{\int_{\mathbb{R}^{N+}} l_1^{k_1} l_2^{k_2} ... l_N^{k_N} f_0(l_1, l_2, \ldots, l_N)\, dl_1 dl_2 \ldots dl_N}{\int_{\mathbb{R}^{N+}} f_0(l_1, l_2, \ldots, l_N)\, dl_1 dl_2 \ldots dl_N} \tag{5}$$

The mixed pathlength moment of order $k_1 + k_2 + \cdots + k_N$ can be also defined as:

$$\langle l_1^{k_1} l_2^{k_2} \ldots l_N^{k_N} \rangle_\phi = \frac{(-1)^{k_1+k_2+\ldots+k_N}}{G_{\phi_0}(\mathbf{r}_0 \to \mathbf{r})} \frac{\partial^{k_1+k_2+\ldots+k_N} G_{\phi_0}(\mathbf{r}_0 \to \mathbf{r})}{\partial\mu_{a_1}^{k_1} \ldots \partial\mu_{a_N}^{k_N}} \tag{6}$$

We can find an expression for the moments by solving the perturbative CW RTE[21] which relates the change of absorption $\Delta\mu_a(\mathbf{r})$ to the change in the radiance between an initial ($\mathfrak{L}_0$) and a perturbed state ($\mathfrak{L}_p$), $\Delta\mathfrak{L}(\mathbf{r}, \hat{\mathbf{s}}) = \mathfrak{L}_p(\mathbf{r}, \hat{\mathbf{s}}) - \mathfrak{L}_0(\mathbf{r}, \hat{\mathbf{s}})$:

$$\hat{\mathbf{s}} \cdot \nabla [\Delta\mathfrak{L}(\mathbf{r}, \hat{\mathbf{s}})] + \mu_t(\mathbf{r})\, \Delta\mathfrak{L}(\mathbf{r}, \hat{\mathbf{s}}) = \mu_s(\mathbf{r}) \int_{4\pi} p(\hat{\mathbf{s}}' \to \hat{\mathbf{s}})\, \Delta\mathfrak{L}(\mathbf{r}, \hat{\mathbf{s}}')\, d\hat{\mathbf{s}}' - \Delta\mu_a(\mathbf{r})\, \mathfrak{L}_p(\mathbf{r}, \hat{\mathbf{s}}) \tag{7}$$

where $\mathfrak{L}(\mathbf{r}, \hat{\mathbf{s}})$ is the radiance, i.e., the number of photons travelling along the direction $\hat{\mathbf{s}}$ per unit time, per unit area orthogonal to $\hat{\mathbf{s}}$, per unit solid angle ($[\mathfrak{L}] = \mathrm{L}^{-2}\mathrm{Sr}^{-1}\mathrm{T}^{-1}$), which depends on both spatial ($\mathbf{r}$) and angular ($\hat{\mathbf{s}}$) variables; $p(\hat{\mathbf{s}}' \to \hat{\mathbf{s}})$ is the phase function ($[p] = \mathrm{Sr}^{-1}$). Also, $\mu_t = \mu_a + \mu_s$ where, $\mu_t$, $\mu_s$ and $\mu_a$ are the extinction, scattering and absorption coefficients, respectively. If the RTE for the initial and perturbed state have

a source term $S(\mathbf{r},\widehat{\mathbf{s}}) = \delta(\mathbf{r}-\mathbf{r}_0)\,\delta(\widehat{\mathbf{s}}-\widehat{\mathbf{s}}_0)$, the solution of Eq. (7) is known as the Dyson equation for the Green's function of the radiance[29]:

$$G_{\mathfrak{L}_p}(\mathbf{r}_0,\widehat{\mathbf{s}}_0\to\mathbf{r},\widehat{\mathbf{s}}) = G_{\mathfrak{L}_0}(\mathbf{r}_0,\widehat{\mathbf{s}}_0\to\mathbf{r},\widehat{\mathbf{s}}) - \int_V d\mathbf{r}'\int_{4\pi}\Delta\mu_a(\mathbf{r}')\,G_{\mathfrak{L}_p}(\mathbf{r}_0,\widehat{\mathbf{s}}_0\to\mathbf{r}',\widehat{\mathbf{s}}')\,G_{\mathfrak{L}_0}(\mathbf{r}',\widehat{\mathbf{s}}'\to\mathbf{r},\widehat{\mathbf{s}})\,d\widehat{\mathbf{s}}' \quad (8)$$

where $G_{\mathfrak{L}}(\mathbf{r}_0,\widehat{\mathbf{s}}_0\to\mathbf{r},\widehat{\mathbf{s}})$ is the Green's function of the radiance that is found at $\mathbf{r}$ in the direction $\widehat{\mathbf{s}}$ when light is emitted at $\mathbf{r}_0$ in the direction $\widehat{\mathbf{s}}_0$ ($[G_{\mathfrak{L}}] = \mathrm{L}^{-2}\mathrm{Sr}^{-1}$). We note that the same method can also be used for the perturbative DE[21,30].

The solution of the Dyson equation is expressed by the Neumann series[31–33]. Each order of the Neumann series can be integrated over the solid angle $\widehat{\mathbf{s}}$ which provides the corresponding order of approximation for $G_{\phi_p}(\mathbf{r}_0,\widehat{\mathbf{s}}_0\to\mathbf{r})$ (i.e., the Green's function of the fluence rate at $\mathbf{r}$). Comparison with Eq. (4) allows one to find the expression of the moments. We will provide the expression for a general mixed moment for the Dyson equation of the DE (see Eq. 13). For the RTE, it will suffice to find the first order moment, which corresponds to the first order of the Neumann series. For an isotropic source $S(\mathbf{r},\widehat{\mathbf{s}}) = \frac{1}{4\pi}\delta(\mathbf{r}-\mathbf{r}_0)$, the corresponding Green's function for the radiance will be $G_{\mathfrak{L}_{iso}}(\mathbf{r}_0\to\mathbf{r},\widehat{\mathbf{s}}) = \frac{1}{4\pi}\int_{4\pi}G_{\mathfrak{L}}(\mathbf{r}_0,\widehat{\mathbf{s}}'\to\mathbf{r},\widehat{\mathbf{s}})\,d\widehat{\mathbf{s}}'$. For a uniform change of absorption in the region $V$, the first order term of the Neumann series yields (from Eq. 8):

$$G_{\mathfrak{L}_{p,iso}}(\mathbf{r}_0\to\mathbf{r},\widehat{\mathbf{s}}) = G_{\mathfrak{L}_{0,iso}}(\mathbf{r}_0\to\mathbf{r},\widehat{\mathbf{s}}) - \Delta\mu_a\int_V d\mathbf{r}'\int_{4\pi}G_{\mathfrak{L}_{0,iso}}(\mathbf{r}_0\to\mathbf{r}',\widehat{\mathbf{s}}')\,G_{\mathfrak{L}_0}(\mathbf{r}',\widehat{\mathbf{s}}'\to\mathbf{r},\widehat{\mathbf{s}})\,d\widehat{\mathbf{s}}' \quad (9)$$

Integration of Eq. (9) over the angular variable $\widehat{\mathbf{s}}$ yields:

$$\Delta G_\phi(\mathbf{r}_0\to\mathbf{r}) = -\Delta\mu_a\int_V d\mathbf{r}'\int_{4\pi}d\widehat{\boldsymbol{s}}\int_{4\pi}G_{\mathfrak{L}_{0,iso}}(\mathbf{r}_0\to\mathbf{r}',\widehat{\mathbf{s}}')\,G_{\mathfrak{L}_0}(\mathbf{r}',\widehat{\mathbf{s}}'\to\mathbf{r},\widehat{\mathbf{s}})\,d\widehat{\mathbf{s}}' \quad (10)$$

where $\Delta G_\phi(\mathbf{r}_0\to\mathbf{r}) = G_{\phi_p}(\mathbf{r}_0\to\mathbf{r}) - G_{\phi_0}(\mathbf{r}_0\to\mathbf{r})$.

By using Eqs. (6) and (10) we obtain:

$$\langle l_i\rangle_\phi = \lim_{\Delta\mu_{ai}\to 0} -\frac{1}{G_{\phi_0}(\mathbf{r}_0\to\mathbf{r})}\frac{\Delta G_\phi(\mathbf{r}_0\to\mathbf{r})}{\Delta\mu_{ai}} = \frac{\int_{V_i}d\mathbf{r}'\int_{4\pi}d\hat{\mathbf{s}}\int_{4\pi}G_{\mathfrak{L}_{0,iso}}(\mathbf{r}_0\to\mathbf{r}',\hat{\mathbf{s}}')\,G_{\mathfrak{L}_0}(\mathbf{r}',\hat{\mathbf{s}}'\to\mathbf{r},\hat{\mathbf{s}})\,d\hat{\mathbf{s}}'}{G_{\phi_0}(\mathbf{r}_0\to\mathbf{r})} \quad (11)$$

where $\langle l_i\rangle_\phi$ is the average pathlength spent in the region of interest when photons are emitted from $\mathbf{r}_0$ and later found at $\mathbf{r}$. We name this type of partial pathlength as fluence rate partial pathlength. It is also the absorption Jacobian of the logarithmic Green's function, $\ln\left(\frac{G_\phi(\mathbf{r}_0\to\mathbf{r})}{\Psi_{ref}}\right)$, where $\Psi_{ref}$ is an arbitrary reference intensity per unit source power ($[\Psi_{ref}] = \mathrm{L}^{-2}$). If we can assume that under certain conditions of highly diffusive media $G_{\mathfrak{L}_0}(\mathbf{r}',\widehat{\mathbf{s}}'\to\mathbf{r},\widehat{\mathbf{s}}) \approx G_{\mathfrak{L}_{0,iso}}(\mathbf{r}'\to\mathbf{r},\widehat{\mathbf{s}})$, or $G_{\mathfrak{L}_{0,iso}}(\mathbf{r}_0\to\mathbf{r}',\widehat{\mathbf{s}}') \approx \frac{1}{4\pi}G_{\phi_0}(\mathbf{r}_0\to\mathbf{r}')$ (or both) then we can decouple the two Green's functions in Eq. (11) and carry out the two angular integrations separately. In this way we obtain:

$$\langle l_i\rangle_\phi = \frac{\int_{V_i}G_{\phi_0}(\mathbf{r}_0\to\mathbf{r}')\,G_{\phi_0}(\mathbf{r}'\to\mathbf{r})\,d\mathbf{r}'}{G_{\phi_0}(\mathbf{r}_0\to\mathbf{r})} \quad (12)$$

We shall see in the next section that this expression is also obtained from the Rytov approximation for the DE [We note that more appropriately in DT $G_{\mathfrak{L}_{0,iso}}(\mathbf{r}_0\to\mathbf{r}',\widehat{\mathbf{s}}') \approx \frac{1}{4\pi}G_{\phi_0}(\mathbf{r}_0\to\mathbf{r}') + \frac{3}{4\pi}\mathbf{J}_0(\mathbf{r}_0\to\mathbf{r}')\cdot\widehat{\mathbf{s}}'$, where $\mathbf{J}_0$ is the net flux vector[15]. If we plug this expression into Eq. (11) and we make no assumption for $G_{\mathfrak{L}_0}(\mathbf{r}',\widehat{\mathbf{s}}'\to\mathbf{r},\widehat{\mathbf{s}})$, we will arrive to Eq. (12) with the additional term $-\frac{3}{4\pi G_{\phi_0}(\mathbf{r}_0\to\mathbf{r})}\int_{V_i}\mathbf{J}_0(\mathbf{r}_0\to\mathbf{r}')\cdot\mathbf{J}_0(\mathbf{r}\to\mathbf{r}')\,d\mathbf{r}'$ on the right side. This term is supposed to be negligible with respect to the fluence term].

When diffusion conditions are met, we can solve the perturbative diffusion equation to calculate $G_{\phi_p}(\mathbf{r}_0\to\mathbf{r})$ by use of the Neumann series. The general expression of the mixed pathlength moment of order $n = k_1 + k_2 + .. + k_m$ involving $m$ regions ($m \le N$) is given by Sassaroli et al.[21]:

$$\langle l_1^{k_1}l_2^{k_2}\ldots l_m^{k_m}\rangle_\phi = \frac{k_1!k_2!\ldots k_m!}{G_{\phi_0}(\mathbf{r}_0\to\mathbf{r})}\sum_{\wp(i_1,i_2,\ldots,i_n)}\int_{V_{i_1}}G_{\phi_0}(\mathbf{r}_0\to\mathbf{r}_{i_1})\,G_{\phi_0}(\mathbf{r}_{i_1}\to\mathbf{r}_{i_2})\,d\mathbf{r}_{i_1}\int_{V_{i_2}}G_{\phi_0}(\mathbf{r}_{i_2}\to\mathbf{r}_{i_3})\,d\mathbf{r}_{i_2}\times\cdots\times\int_{V_{i_{n-1}}}G_{\phi_0}(\mathbf{r}_{i_{n-1}}\to\mathbf{r}_{i_n})\,d\mathbf{r}_{i_{n-1}}\int_{V_{i_n}}G_{\phi_0}(\mathbf{r}_{i_n}\to\mathbf{r})\,d\mathbf{r}_{i_n} \quad (13)$$

where $\wp(i_1,i_2,\ldots,i_n)$ is the permutation of $n$ integers with repetitions. The first $k_1$ integers $i_1,i_2,\ldots,i_{k_1}$ are assigned to region "1" ($i_1 = i_2 = \cdots = i_{k_1} = 1$), the next $k_2$ indices are assigned to region "2" ($i_{k_1+1} = i_{k_1+2} = \cdots = i_{k_1+k_2} = 2$), etc. Therefore, the number of permutations is $\frac{n!}{k_1!k_2!\ldots k_m!}$. Further, $G_{\phi_0}(\mathbf{r}_i\to\mathbf{r}_j)$ is the Green's function for the fluence rate for a source at $\mathbf{r}_i$ and a field point at $\mathbf{r}_j$. The mixed moment of Eq. (13) is a measure of the interaction between different points of the medium. It can be thought as proportional to the probability that a photon emitted at $\mathbf{r}_0$ and found at $\mathbf{r}$ will visit $k_1$ points of region 1, $k_2$ points of region 2 etc. The normalization is provided by the probability that a photon emitted at $\mathbf{r}_0$ and found

at $\mathbf{r}$ will visit $n$ points ($n = k_1 + k_2 + .. + k_m$) of the whole medium. Another way to rephrase the previous statement is in terms of the number of scattering events. We note that Eq. (12) is a particular case of Eq. (13), as expected. We also note that Eq. (13) is formally valid also for the moments obtained under the validity of the RTE, if we substitute $G_{\phi_0}\left(\mathbf{r}_{i_j} \rightarrow \mathbf{r}_{i_{j+1}}\right)$ with $G_{\mathfrak{L}_0}\left(\mathbf{r}_{i_j}, \widehat{\mathbf{s}}_{i_j} \rightarrow \mathbf{r}_{i_{j+1}}, \widehat{\mathbf{s}}_{i_{j+1}}\right)$ and integration is carried out over both spatial and angular domains.

In this work we choose to focus on the simple situation where one region is subject to a uniform absorption change $\Delta\mu_{ai}$. Therefore, from Eq. (4) we have:

$$G_{\phi_p}\left(\mathbf{r}_0 \rightarrow \mathbf{r}\right) = G_{\phi_0}\left(\mathbf{r}_0 \rightarrow \mathbf{r}\right) \sum_{k=0}^{\infty} (-1)^k \frac{\langle l_i^k \rangle_\phi}{k!} {\Delta\mu_{ai}}^k \tag{14}$$

where $\langle l_i^k \rangle_\phi$ is the self-moment of order $k$, which is proportional to the probability that a photon emitted at $\mathbf{r}_0$ and found at $\mathbf{r}$ visits $k$ points of the region of interest. We note that the expression of $\langle l_i^k \rangle_\phi$ is included in the general expression of a mixed moment (Eq. 13). For reflectance calculations, $R_p\left(\mathbf{r}_0 \rightarrow \mathbf{r}\right)$ has the same form of Eq. (14) but with $G_{\phi_0}\left(\mathbf{r}_0 \rightarrow \mathbf{r}\right)$ replaced by $R_0\left(\mathbf{r}_0 \rightarrow \mathbf{r}\right)$, and $\langle l_i^k \rangle_\phi$ replaced by $\langle l_i^k \rangle_R$[21]. The general expression of the mixed moment of Eq. (13) is also valid for reflectance calculations with the only substitution of the last integrand $G_{\phi_0}\left(\mathbf{r}_{i_n} \rightarrow \mathbf{r}\right)$ with $R_0\left(\mathbf{r}_{i_n} \rightarrow \mathbf{r}_b\right)$, where $\mathbf{r}_b$ is a boundary point where the detector is located.

## Born and Rytov approximations and their physical meaning

Equation (14) is valid for arbitrary changes of the absorption coefficient, however, more commonly the perturbative diffusion equation is solved according to the Born or Rytov approximations, which assume small changes in the absorption coefficient. The Born approximation assumes that $\Delta G_\phi\left(\mathbf{r}_0 \rightarrow \mathbf{r}\right) = G_{\phi_p}\left(\mathbf{r}_0 \rightarrow \mathbf{r}\right) - G_{\phi_0}\left(\mathbf{r}_0 \rightarrow \mathbf{r}\right) \ll G_{\phi_0}\left(\mathbf{r}_0 \rightarrow \mathbf{r}\right)$[15]. In other words, the change in the Green's function should be much smaller than the unperturbed value. This is equivalent to retaining the first order expansion of Eq. (14) (i.e., infinitesimal changes of the absorption coefficient):

$$G_{\phi_p}\left(\mathbf{r}_0 \rightarrow \mathbf{r}\right) \approx G_{\phi_0}\left(\mathbf{r}_0 \rightarrow \mathbf{r}\right)\left[1 - \langle l_i \rangle_\phi \Delta\mu_{ai}\right] \tag{15}$$

The Rytov approximation seeks a solution to the diffusion equation of the type:

$$G_{\phi_p}\left(\mathbf{r}_0 \rightarrow \mathbf{r}\right) = G_{\phi_0}\left(\mathbf{r}_0 \rightarrow \mathbf{r}\right) e^{-\psi\left(\mathbf{r}_0, \mathbf{r}\right)} \tag{16}$$

After some calculations (Supplementary Information S1) we arrive to the expression for the exponent:

$$\psi\left(\mathbf{r}_0, \mathbf{r}\right) = \frac{1}{G_{\phi_0}\left(\mathbf{r}_0 \rightarrow \mathbf{r}\right)} \int_{V'} G_{\phi_0}\left(\mathbf{r}_0 \rightarrow \mathbf{r}'\right) \left\{\Delta\mu_a\left(\mathbf{r}'\right) - \left[D\left(\mathbf{r}'\right) \left\|\nabla\psi\left(\mathbf{r}_0, \mathbf{r}'\right)\right\|^2\right]\right\} G_{\phi_0}\left(\mathbf{r}' \rightarrow \mathbf{r}\right) d\mathbf{r}' \tag{17}$$

The assumption of the Rytov approximation is to neglect $D\left(\mathbf{r}'\right) \left\|\nabla\psi\left(\mathbf{r}_0, \mathbf{r}'\right)\right\|^2$ in the integrand, therefore we obtain (for $\Delta\mu_a\left(\mathbf{r}'\right) = \Delta\mu_{ai}$):

$$\psi\left(\mathbf{r}_0, \mathbf{r}\right) = \frac{\Delta\mu_{ai}}{G_{\phi_0}\left(\mathbf{r}_0 \rightarrow \mathbf{r}\right)} \int_{V'} G_{\phi_0}\left(\mathbf{r}_0 \rightarrow \mathbf{r}'\right) G_{\phi_0}\left(\mathbf{r}' \rightarrow \mathbf{r}\right) d\mathbf{r}' = \langle l_i \rangle_\phi \Delta\mu_{ai} \tag{18}$$

The formula derived by the Rytov approximation for the exponent yields the product of the fluence rate partial pathlength and the change in the absorption coefficient.

Now we observe that Eq. (16) can be rewritten as:

$$G_{\phi_p}\left(\mathbf{r}_0 \rightarrow \mathbf{r}\right) = G_{\phi_0}\left(\mathbf{r}_0 \rightarrow \mathbf{r}\right) e^{-\langle l_i \rangle_\phi \Delta\mu_{ai}} = G_{\phi_0}\left(\mathbf{r}_0 \rightarrow \mathbf{r}\right) \sum_{k=0}^{\infty} (-1)^k \frac{\langle l_i \rangle_\phi^k}{k!} {\Delta\mu_{ai}}^k \tag{19}$$

Three important considerations follow: (1) the Rytov approximation (unlike the Born approximation) is not linear with $\Delta\mu_{ai}$, therefore it can describe some nonlinear effects due to absorption changes (see section "Calculations of reflectance perturbation due to a strong localized absorption change"); (2) by comparing Eqs. (19) and (14) the physical approximation inherent in the Rytov approximation is that $\langle l_i^k \rangle_\phi$ can be substituted by $\langle l_i \rangle_\phi^k$. This assumption is usually a poor one and leads to miscalculations for large values of $\Delta\mu_{ai}$ (see section "Calculations of reflectance perturbation due to a strong localized absorption change"). (3) We can easily verify that the Born and Rytov approximations coincide when $\Delta\mu_{ai} \rightarrow 0$ i.e., when only the first term of Eq. (14) is retained.

In conclusion, the Rytov approximation has the natural physical interpretation that its exponent is the product of the fluence rate partial pathlength times the change of the absorption coefficient in a region of interest. Therefore Eq. (19) shows an elegant link between the Rytov approximation and Beer–Lambert law for

clear media when a change of the absorption coefficient occurs in a region of the medium: $I_d = I_0 e^{-L_i \Delta\mu_{ai}}$, where $I_0$ and $I_d$ are the detected intensities before and after the absorption change ($\Delta\mu_{ai}$), respectively, and $L_i$ is the direct pathlength of photons crossing the region. We can see that they are formally the same equation with the substitution of $L_i$ with $\langle l_i \rangle_\phi$. Equation (19) also implies that for the calculation of perturbations of the fluence rate due to absorption changes, higher order terms of the series (Eq. 19) depend on $\langle l_i \rangle_\phi^k$ instead of $\langle l_i^k \rangle_\phi$ (Eq. 14).

## Calculation of reflectance based on Born and Rytov approximations

Now we address the calculation of the reflectance under the Born and Rytov approximations by using Fick's law: $R_p(\mathbf{r}_0 \to \mathbf{r}_b) = -D(\mathbf{r}_b) \nabla G_{\phi_p}(\mathbf{r}_0 \to \mathbf{r})_{|\mathbf{r}=\mathbf{r}_b} \cdot \widehat{\mathbf{n}}(\mathbf{r}_b)$, where $\widehat{\mathbf{n}}(\mathbf{r}_b)$ is the unit outward vector at the boundary point $\mathbf{r}_b$. This means that we assume a detector at $\mathbf{r}_b$ with a 90° acceptance angle. When the fluence rate is obtained from the Born approximation (Eq. 15), by carrying out the gradient and considering the expression for $\langle l_i \rangle_\phi$ (Eq. 12) we obtain:

$$R_p(\mathbf{r}_0 \to \mathbf{r}_b) = R_0(\mathbf{r}_0 \to \mathbf{r}_b) \left[1 - \langle l_i \rangle_R \Delta\mu_{ai}\right] \tag{20}$$

Therefore, the Born approximation for the reflectance has the same form as for the fluence rate, except the mean pathlength in the region of interest is considered for photons exiting the medium (i.e., $\langle l_i \rangle_R$). The expression for $\langle l_i \rangle_R$ is easily obtained by applying Fick's law to Eq. (15):

$$\langle l_i \rangle_R = \frac{1}{R_0(\mathbf{r}_0 \to \mathbf{r}_b)} \int_{V'} G_{\phi_0}(\mathbf{r}_0 \to \mathbf{r}') R_0(\mathbf{r}' \to \mathbf{r}_b) \, d\mathbf{r}' \tag{21}$$

here, $R_0(\mathbf{r}' \to \mathbf{r}_b)$ is the reflectance for a point source at $\mathbf{r}'$ calculated at $\mathbf{r}_b$. When the fluence rate is obtained from Rytov approximation, after some calculations (Supplementary Information S2) we obtain:

$$R_p(\mathbf{r}_0 \to \mathbf{r}_b) = R_0(\mathbf{r}_0 \to \mathbf{r}_b) e^{-\psi(\mathbf{r}_0, \mathbf{r})} \left[1 - \Delta\mu_{ai} \left(\langle l_i \rangle_R - \langle l_i \rangle_\phi\right)\right] \tag{22}$$

where, $\psi(\mathbf{r}_0, \mathbf{r})$ is given by Eq. (18). Therefore, the Rytov approximation for the reflectance has the same form as for the fluence rate *only if* $\langle l_i \rangle_R = \langle l_i \rangle_\phi$. Even though the expressions of these mean pathlengths are distinct, when $\mathbf{r} = \mathbf{r}_b$ their values can be very close to each other. In fact, for the calculation of $\langle l_i \rangle_\phi$ we consider the average pathlengths of photons emitted at $\mathbf{r}_0$ that cross the region of interest and are found at $\mathbf{r}_b$. A subset of these photons will exit the medium at the same point, and it can be anticipated that the average pathlength calculated from this subset (which is $\langle l_i \rangle_R$) yields similar values in several situations of interest in diffuse optics. Even from the standpoint of MC simulations these two pathlengths have distinct definitions. If we consider a photon visiting a field point $\mathbf{r}$ as "detected" in terms of fluence rate, the main difference between fluence rate and reflectance pathlengths is that a photon can be detected multiple times for fluence rate measurements, but only one time for reflectance measurements (Supplementary Information S3). These considerations also highlight, by directly reasoning with the physics of photon migration, the approximate nature of the PCBC used for solving DE. According to this boundary condition we would have $\langle l_i \rangle_R = \langle l_i \rangle_\phi$, and the form of Rytov approximation for the reflectance perturbation would be the same as the Rytov approximation itself (Eq. 16). This is the most common approach adopted in the literature.

We also note that the expressions for the perturbed reflectance obtained under Born approximation (Eq. 20) and Rytov approximation (Eq. 22) coincide when $\Delta\mu_{ai} \to 0$. In fact, Eq. (22) can be rewritten as:

$$\ln\left(\frac{R_p(\mathbf{r}_0 \to \mathbf{r}_b)}{R_0(\mathbf{r}_0 \to \mathbf{r}_b)}\right) = -\psi(\mathbf{r}_s, \mathbf{r}) + \ln\left\{\left[1 - \Delta\mu_{ai}\left(\langle l_i \rangle_R - \langle l_i \rangle_\phi\right)\right]\right\} \tag{23}$$

When $\Delta\mu_{ai} \to 0$ and $R_p(\mathbf{r}_0 \to \mathbf{r}_b) \to R_0(\mathbf{r}_0 \to \mathbf{r}_b)$, by taking the Taylor expansion of the logarithms of Eq. (22) we have that:

$$\frac{R_p(\mathbf{r}_0 \to \mathbf{r}_b)}{R_0(\mathbf{r}_0 \to \mathbf{r}_b)} - 1 = -\langle l_i \rangle_R \Delta\mu_{ai} \tag{24}$$

which is Eq. (20). Of course, this is true also for the perturbed fluence rates obtained under the Born and Rytov approximations, which in the limit $\Delta\mu_{ai} \to 0$ must coincide.

## Relationship between the correct forward-adjoint method and the present work

The main advantage of the coupled forward-adjoint method is to reduce the variance of the estimate of the absorption Jacobians in general situations where RTE is valid[17,18]. The method is also efficient because it allows one to provide a map of the absorption sensitivities in a region of interest by using only two MC simulations for each source-detector pair. The method relies on the reciprocity theorem in the RTE[34] $G_{\mathfrak{L}_0}(\mathbf{r}_1, \widehat{\mathbf{s}}_1 \to \mathbf{r}_2, \widehat{\mathbf{s}}_2) = G_{\mathfrak{L}_0}(\mathbf{r}_2, -\widehat{\mathbf{s}}_2 \to \mathbf{r}_1, -\widehat{\mathbf{s}}_1)$ which describes the reversibility of light paths. For a

medium with varying refractive index the theorem has a modified form[35]. To see the importance of the adjoint method, let us consider a case where the physical quantity of interest is the fluence rate at a point $\mathbf{r}$ (detector) when photons are emitted isotropically at $\mathbf{r}_0$ (source). The traditional method to calculate the absorption Jacobian at a region of interest is to propagate the photons from the source and calculate the pathlength travelled by each photon in the region of interest ($\mathbf{r}'$). This number is stored in memory and will be used only if a photon reaches the detector ($\mathbf{r}$). Therefore, depending on the details of the simulation (i.e., size of the region of interest, size of source and detector, source-detector distance, optical properties of the medium) much of the computation will not be used because only a small fraction of the photons that intersect the region of interest are detected. To alleviate this problem, we can use the reciprocity theorem in Eq. (11) which we rewrite as follows:

$$\langle l_i \rangle_\phi = \frac{\int_{V_i} d\mathbf{r}' \int_{4\pi} d\widehat{\boldsymbol{s}} \int_{4\pi} G_{\mathfrak{L}_{0,iso}} (\mathbf{r}_0 \rightarrow \mathbf{r}', \widehat{\mathbf{s}}')\, G_{\mathfrak{L}_0} (\mathbf{r}, -\widehat{\mathbf{s}} \rightarrow \mathbf{r}', -\widehat{\mathbf{s}}')\, d\widehat{\mathbf{s}}'}{G_{\phi_0} (\mathbf{r}_0 \rightarrow \mathbf{r})} = \frac{4\pi \int_{V_i} d\mathbf{r}' \int_{4\pi} G_{\mathfrak{L}_{0,iso}} (\mathbf{r}_0 \rightarrow \mathbf{r}', \widehat{\mathbf{s}}')\, G_{\mathfrak{L}_{0,iso}} (\mathbf{r} \rightarrow \mathbf{r}', -\widehat{\mathbf{s}}')\, d\widehat{\mathbf{s}}'}{G_{\phi_0} (\mathbf{r}_0 \rightarrow \mathbf{r})} \tag{25}$$

and thus:

$$\langle l_i \rangle_\phi = \frac{4\pi \int_{V_i} d\mathbf{r}' \int_{4\pi} G_{\mathfrak{L}_{0,iso}} (\mathbf{r}_0 \rightarrow \mathbf{r}', \widehat{\mathbf{s}}')\, G^\star_{\mathfrak{L}_{0,iso}} (\mathbf{r} \rightarrow \mathbf{r}', \widehat{\mathbf{s}}')\, d\widehat{\mathbf{s}}'}{G_{\phi_0} (\mathbf{r}_0 \rightarrow \mathbf{r})} \tag{26}$$

where $G^\star_{\mathfrak{L}_{0,iso}} (\mathbf{r} \rightarrow \mathbf{r}', \widehat{\mathbf{s}}')$ is the solution of the adjoint RTE equation for an isotropic point source at $\mathbf{r}$[17,18]. This equation governs the radiance when the roles of source and detectors are swapped. We can see from Eqs. (25) and (26) that we achieve our goal by multiplying two Green's functions' fields: one from the source at $\mathbf{r}_0$ to the region of interest at $\mathbf{r}'$ in the direct simulation ($G_{\mathfrak{L}_{0,iso}} (\mathbf{r}_0 \rightarrow \mathbf{r}', \widehat{\mathbf{s}}')$), and the other from the detector at $\mathbf{r}$ to the region of interest at $\mathbf{r}'$ in the adjoint simulation ($G^\star_{\mathfrak{L}_{0,iso}} (\mathbf{r} \rightarrow \mathbf{r}', \widehat{\mathbf{s}}')$). In this situation any photon that reaches the region of interest in the two simulations counts for the calculation of the Jacobian. We note that Eq. (26), apart from the normalization, has the same form as in the work of Gardner, 2014 Eq. (4)[18]. Also, with our approach, the interrogation density function proposed by Hayakawa, 2007 Eq. (5.1)[17] has a straightforward physical interpretation as the ratio of partial over total mean pathlengths: $\langle l_i \rangle_\phi / \langle L \rangle_\phi$ and $\langle l_i \rangle_R / \langle L \rangle_R$ for fluence rate and reflectance measurements, respectively. These ratios are naturally normalized to 1 when we integrate over the whole medium. We note that for the calculation of $\langle l_i \rangle_R$ one must also consider the refractive index mismatch between the diffusive and the outer medium. The general formula for $\langle l_i \rangle_R$ for an isotropic point source at $\mathbf{r}_0$ is:

$$\langle l_i \rangle_R = \frac{\int_{V_i} d\mathbf{r}' \int_\Omega \left[1 - r_{io} (\widehat{\mathbf{s}} \cdot \widehat{\mathbf{n}})\right] \widehat{\mathbf{s}} \cdot \widehat{\mathbf{n}} d\widehat{\boldsymbol{s}} \int_{4\pi} G_{\mathfrak{L}_{0,iso}} (\mathbf{r}_0 \rightarrow \mathbf{r}', \widehat{\mathbf{s}}')\, G_{\mathfrak{L}_0} (\mathbf{r}', \widehat{\mathbf{s}}' \rightarrow \mathbf{r}_b, \widehat{\mathbf{s}})\, d\widehat{\mathbf{s}}'}{\int_\Omega \left[1 - r_{io} (\widehat{\mathbf{s}} \cdot \widehat{\mathbf{n}})\right] G_{\mathfrak{L}_{0,iso}} (\mathbf{r}_0 \rightarrow \mathbf{r}_b, \widehat{\mathbf{s}})\, \widehat{\mathbf{s}} \cdot \widehat{\mathbf{n}} d\widehat{\boldsymbol{s}}} \tag{27}$$

where $\Omega$ is the acceptance angle of the detector in the medium, $\widehat{\mathbf{n}}$ the unit vector directed outward to the medium at the location of the detector ($\widehat{\mathbf{s}} \cdot \widehat{\mathbf{n}} \geq 0$), and $r_{io}$ is the reflection coefficient for unpolarized light for photons propagating from the diffusive to the outer medium. Here for simplicity, we have considered a point detector (at $\mathbf{r}_b$). Even for reflectance calculations a map of the absorption sensitivity can be obtained by using only a direct and an adjoint MC simulation. Before describing these two simulations, we note that in general the two angular integrals of Eq. (27) cannot be decoupled. Under diffusion conditions the decoupling is possible (see section "A random multivariate approach to perturbation theory of photon transport"), and Eq. (27) reduces to Eq. (21). In this situation the direct simulation is used for the calculation of $G_{\mathfrak{L}_{0,iso}} (\mathbf{r}_0 \rightarrow \mathbf{r}', \widehat{\mathbf{s}}') \approx \frac{1}{4\pi} G_{\phi_0} (\mathbf{r}_0 \rightarrow \mathbf{r}')$ and the denominator of Eq. (27), i.e., $R_0 (\mathbf{r}_0 \rightarrow \mathbf{r}_b)$. The adjoint simulation is used for estimating $R_0 (\mathbf{r}' \rightarrow \mathbf{r}_b)$ (Eq. 21), which is obtained by the Green's function $G_{\mathfrak{L}_0} (\mathbf{r}', \widehat{\mathbf{s}}' \rightarrow \mathbf{r}_b, \widehat{\mathbf{s}})$ of Eq. (27), by considering that $G_{\mathfrak{L}_0} (\mathbf{r}', \widehat{\mathbf{s}}' \rightarrow \mathbf{r}_b, \widehat{\mathbf{s}}) \approx G_{\mathfrak{L}_{0,iso}} (\mathbf{r}' \rightarrow \mathbf{r}_b, \widehat{\mathbf{s}})$. The appropriate adjoint simulation to calculate $R_0 (\mathbf{r}' \rightarrow \mathbf{r}_b)$ at all points $\mathbf{r}'$, is again obtained by using the reciprocity theorem: $G_{\mathfrak{L}_0} (\mathbf{r}', \widehat{\mathbf{s}}' \rightarrow \mathbf{r}_b, \widehat{\mathbf{s}}) = G_{\mathfrak{L}_0} (\mathbf{r}_b, -\widehat{\mathbf{s}} \rightarrow \mathbf{r}', -\widehat{\mathbf{s}}')$. Integration over $\widehat{\mathbf{s}}'$ in Eq. (27) yields $G_{\phi_0} (\mathbf{r}_b, -\widehat{\mathbf{s}} \rightarrow \mathbf{r}')$. Therefore, we can provide the following "recipe" for the adjoint MC simulation: we inject the photons in the medium at $\mathbf{r}_b$ isotropically within the acceptance angle $\Omega$; each photon is assigned a weight $w = \frac{1}{4\pi} \left[1 - r_{io} (\widehat{\mathbf{s}} \cdot \widehat{\mathbf{n}})\right] \widehat{\mathbf{s}} \cdot \widehat{\mathbf{n}}$, and its contribution to the fluence rate at $\mathbf{r}'$ is calculated. In the expression of $w$ the effect of the refractive index mismatch is considered in the factor $w_r = \left[1 - r_{io} (\widehat{\mathbf{s}} \cdot \widehat{\mathbf{n}})\right]$. Alternatively, one can use random numbers to decide if an emitted photon is either reflected or transmitted in the medium. In both cases, the number of emitted photons is used for normalization. We point out that the adjoint simulation does not require the knowledge of the exact angular distribution of the detected radiance in the direct simulation, but only the knowledge of the spatial and angular features of the detector.

## Methods

Both diffusion theory (DT) calculations and MC simulations were obtained for nine combinations of the optical properties in a semi-infinite medium geometry. The values of the absorption coefficient were: $\mu_a = (0.005, 0.01, 0.02)\ \text{mm}^{-1}$, while the values of the reduced scattering coefficient were: $\mu'_s = (0.5, 1, 1.5)\ \text{mm}^{-1}$. The reduced albedo ($\frac{\mu'_s}{\mu'_s + \mu_a}$) covered the range (0.961, 0.997), where the first and last endpoints correspond to $(\mu_a, \mu'_s) = (0.02, 0.5)\ \text{mm}^{-1}$ and $(\mu_a, \mu'_s) = (0.005, 1.5)\ \text{mm}^{-1}$, respectively.

## Diffusion theory calculations

The partial pathlength in a region of interest was calculated for exiting photons (here defined as reflectance pathlengths, $\langle l_i \rangle_R$) or for photons crossing an observation point inside the medium or at its boundary (here defined as fluence rate pathlengths $\langle l_i \rangle_\phi$). The formulas used for the two cases are:

$$\langle l_i \rangle_R = \frac{\int_V G_{\phi_0}(\mathbf{r}_0 \to \mathbf{r}')\, R_0(\mathbf{r}' \to \mathbf{r}_b)\, d\mathbf{r}'}{R_0(\mathbf{r}_0 \to \mathbf{r}_b)} \tag{28}$$

and

$$\langle l_i \rangle_\phi = \frac{\int_V G_{\phi_0}(\mathbf{r}_0 \to \mathbf{r}')\, G_{\phi_0}(\mathbf{r}' \to \mathbf{r}_b)\, d\mathbf{r}'}{G_{\phi_0}(\mathbf{r}_0 \to \mathbf{r}_b)} \tag{29}$$

where $\mathbf{r}_0 = (x_0, y_0, z_0) = (0,0,1/\mu_s')$, is the location of the point source, $\mathbf{r}' = (x', y', z')$ is a point inside the region of interest, $\mathbf{r}_b = (\rho, 0, 0)$ is the position of the detector, and $V$ is the region of interest. $G_{\phi_0}(\mathbf{r}_i \to \mathbf{r}_j)$ is the Green's function of the fluence rate for a point source at $\mathbf{r}_i$ and calculated at $\mathbf{r}_j$. $R_0(\mathbf{r}_i \to \mathbf{r}_b)$ is obtained by Fick's law: $R_0(\mathbf{r}_i \to \mathbf{r}_b) = -D\nabla G_{\phi_0}(\mathbf{r}_i \to \mathbf{r})_{|\mathbf{r}=\mathbf{r}_b}$ (where, $D = \frac{1}{(3\mu_s')}$ is the diffusion coefficient). Extrapolated boundary conditions (EBC) were used for the calculations of $G_{\phi_0}$ and $R_0$ in the semi-infinite medium geometry where the surface is orthogonal to $\hat{z}$ (Fig. 1). The solutions have been given in previous publications[21,36]. While the correct definition of fluence rate partial pathlength at the detector's position implies that $\mathbf{r} = \mathbf{r}_b = (\rho, 0, 0)$ (see Fig. 1), for comparison with MC data we have also used $\mathbf{r} = (\rho, 0, s/2)$ (where $s/2 = 0.5$ mm corresponds to half a voxel size in the MC code MCX; see section "Monte Carlo simulations") and $\mathbf{r} = (\rho, 0, 1/\mu'_s)$.

For the calculations of reflectance change for a wide range of localized absorption changes (see Eq. 14), higher order moments, here considered up to the fourth order, are needed. We used an approximate formula which we have proven to be effective and faster than calculating multiple volume integrals[21]:

$$\langle l_i^n \rangle_R \approx c_{n-1} \langle l_i \rangle_R \left[ \int_V G_{\phi_{0,\infty}}\left(|\mathbf{r}_c - \mathbf{r}'|\right) d\mathbf{r}' \right]^{n-1} \quad n \geq 2 \tag{30}$$

where, $G_{\phi_{0,\infty}}(|\mathbf{r}_c - \mathbf{r}'|)$ is the Green's function of the DE in the infinite medium geometry, when the point source is at the center ($\mathbf{r}_c$) of the region of interest. The factors $c_{n-1}$ ($n = 2, 3, 4$) are numeric quasi-constants (they are rather independent of the optical properties of the medium, the location and partly the size of the region of interest). The values of the numeric quasi-constant are: $c_1 \approx 1.5, c_2 \approx 3.5, c_3 \approx 10$ (see Supplementary information S4). A schematic of the medium, the source-detector system and the regions of interest are shown in Fig. 1.

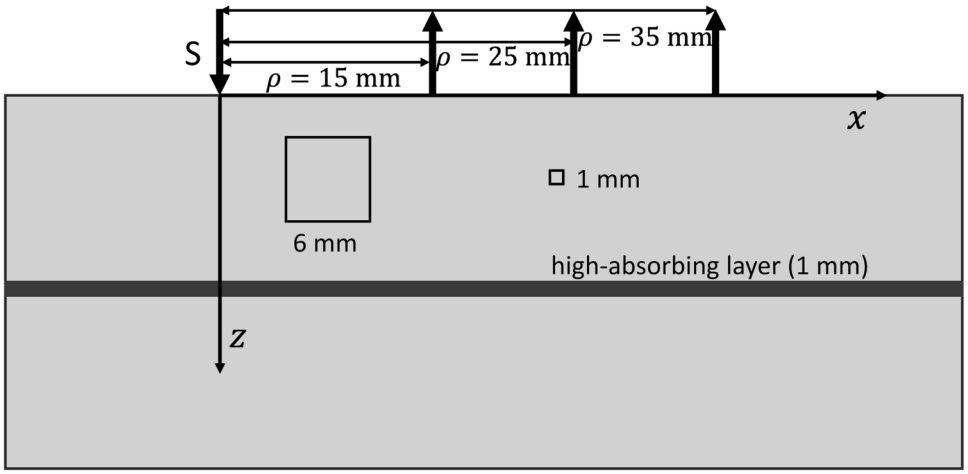


**Fig. 1**. Schematic of the diffusive medium used, featuring one pencil beam source (S) and three detectors at the distance $\rho = 15, 25, 35$ mm. In all the figures (except Figs. 7,8) the medium was homogeneous. For the Figs. 7,8 the medium contained a high-absorbing 1 mm thick layer. Two regions of interest were used: (1) a cube having a side of 6 mm (for the Figs. 2, 3, 9, 10); (2) a cube having a side of 1 mm (for the Figs. 4,5,6,7,8). For the calculation of Jacobians (Figs. 2, 3, 4,5,6,7, 8) the region of interest had the same optical properties of the bulk medium. For the forward problem calculations (Figs. 9, 10), the region of interest had a different absorption coefficient than the bulk medium. The outer and inner refractive indices are $n_o = 1$ and $n_i = 1.4$, respectively.

For the calculations of Eqs. (28), (29), the region of interest was divided in smaller voxels (1 mm side) and for comparison with MC results, we considered detectors of areas that matched those used in MC.

## Monte Carlo simulations

We used two MC codes, one in FORTRAN[37] and MCX (2020 release)[12]. The FORTRAN MC terminated when 100,000 photons were detected in each of the three detectors (Fig. 1). For MCX we launched 1 billion photons and detected a number of photons in the range $(5 \times 10^4, 4.6 \times 10^5)$. Both MCs are white MC codes, i.e., the photons are injected in a non-absorbing medium and the distribution of the absorption coefficient is considered a posteriori by assigning to each detected photon a specific weight. Both MC codes were used for the calculation of $\langle l_i \rangle_R$ according to the formula:

$$\langle l_i \rangle_{R_MC} = \frac{\sum_{j=1}^{n_{total}} l_{ij} e^{-\mu_{ai} l_{ij}} e^{-\mu_{ao} l_{oj}}}{\sum_{j=1}^{n_{total}} e^{-\mu_{ai} l_{ij}} e^{-\mu_{ao} l_{oj}}} \tag{31}$$

where $n_{total}$ is the number of detected photons, $\mu_{ai}$ and $\mu_{ao}$ are the absorption coefficients inside and outside the region of interest, respectively, $l_{ij}$ and $l_{oj}$ are the pathlengths spent inside and outside the region of interest by the $j^{th}$ detected photon, respectively. Note that for the comparison of $\langle l_i \rangle_{R_MC}$ obtained with the two MC codes, we have considered only the case $\mu_{ai} = \mu_{ao}$. On the contrary, for the calculation of reflectance change, we have used both $\mu_{ai} \geq \mu_{ao}$ and $\mu_{ai} \leq \mu_{ao}$. The comparison between the two MC codes was run for the case of isotropic scattering (asymmetry parameter $g = 0$), and an outer and inner refractive index of $n_o = 1$ and $n_i = 1.4$, respectively. For both MCs we considered a pencil beam with the first scattering event occurring along the $z$ axis. Also, we considered detectors of area $(1, 4, 16)\ \mathrm{mm}^2$ at the source-detector separations $\rho = 15, 25, 35$ mm, respectively.

Based on Eq. (29), MCX was also used for the calculation of $\langle l_i \rangle_\phi$ with the following caveats: (1) a pencil beam is used as a source at (0,0,0); the fluence rate calculated by this simulation provides an estimation of $G_{\phi_0}(\mathbf{r}_0 \rightarrow \mathbf{r}')$ in Eq. (29); (2) an isotropic point source is placed in the middle of the first voxel $\mathbf{r} = (\rho, 0, \mathrm{s}/2)$, where s is the voxel size; this allows for the calculation of $G_{\phi_0}(\mathbf{r}' \rightarrow \mathbf{r}_b)$ by use of the reciprocity theorem with the approximation that $\mathbf{r}_b \approx (\rho, 0, \mathrm{s}/2)$; (3) the normalization factor is obtained by the calculation of the fluence rate at $\mathbf{r} = (\rho, 0, \mathrm{s}/2)$ when the source is a pencil beam at (0,0,0). Steps 2) and 3) are also replaced by the following: a pencil beam is placed at the detector position $\mathbf{r}_b = (\rho, 0, 0)$ and is used for evaluating $G_{\phi_0}(\mathbf{r} \rightarrow \mathbf{r}_b)$ of Eq. (29) by the reciprocity theorem. The normalization factor is the fluence rate from the pencil beam at (0,0,0) calculated at a point $\mathbf{r} = (\rho, 0, 1/\mu'_s)$ (denominator of Eq. (29)). The reason for these two methods is because in one case we wanted to apply the correct Rytov approximation which for the adjoint simulation implies an isotropic source placed at the boundary. The best one can do is to place the source at the center of the first voxel. In the other case we were looking for a strategy to obtain the best match with the reflectance mean pathlengths. The MC simulations were carried out for $g = 0.9$. In all the fluence rate calculations, the fluence rates are calculated at the center of a $1\ \mathrm{mm}^3$ voxel and represent the average value inside the voxel. In the figures where MC calculations of $\langle l_i \rangle_\phi$ are shown, we also report $\langle l_i \rangle_{R_MC}$ by the same MCX code. For the calculation of $\langle l_i \rangle_{R_MC}$ the detector's radius was $0.45, 1.8$ mm at the source-detector distance of 15 and 25 mm, respectively; the third receiver, at the distance of 35 mm, had a radius of 4.3 mm for the highest reduced albedo and 6.2 mm for the other combinations. This was done to speed up the convergence of the calculation at the farthest source-detector separation. However, this choice affected the accuracy of the comparisons at this receiver (see discussion in section "Comparison of MCX and diffusion theory results for the calculation of fluence rate and reflectance pathlengths" and the supplementary information S5).

We also used MCX for comparison of $\langle l_i \rangle_\phi$ and $\langle l_i \rangle_{R_MC}$ for a medium with a 1 mm thick highly absorbing layer (mimicking melanin) embedded in it (see Fig. 1). The optical properties of the bulk of the medium and the thin layer were $(\mu_{ab}, \mu'_{sb}) = (0.01, 1)\ \mathrm{mm}^{-1}$ and $(\mu_{a,mel}, \mu'_{s,mel}) = (2, 1)\ \mathrm{mm}^{-1}$, respectively. The absorption of the thin layer can be representative of melanin in epidermis. The source-detector separation was $\rho = 35$ mm and the area of the detector $1\ \mathrm{mm}^2$. The region of interest (for which the Jacobian is calculated) also in this case was a cube of side 1 mm (Fig. 1). To obtain good statistics we injected 130 billion photons.

Last, the FORTRAN MC was used for perturbation calculations with the geometry of Fig. 1 and with the features described at the beginning of this section. For each source-detector separation we calculated the change of reflectance due to a change of the absorption coefficient in a single cubic region (of side 6 mm) half-way between source and detector and at a depth of $z = 12$ mm. The change of absorption coefficient inside the cube spanned the range $\Delta\mu_a \in (-0.02, 0.04)\ \mathrm{mm}^{-1}$.

## Results

In section "Comparison of MC and diffusion theory results for the calculation of reflectance pathlengths" the comparison of MCX[12] and the FORTRAN MC[37] is carried out for the estimation of $\langle l_i \rangle_{R_MC}$. Two cases are shown corresponding to the lowest and the highest reduced albedos. In the same plots $\langle l_i \rangle_R$ (Eq. 28) and $\langle l_i \rangle_\phi$ (Eq. 29) are also shown. In section "Comparison of MCX and diffusion theory results for the calculation of fluence rate and reflectance pathlengths" are shown the comparisons of $\langle l_i \rangle_{R_MC}$ and $\langle l_i \rangle_\phi$, the latter obtained with both MCX and diffusion theory by using Eq. (29). In this section we also considered the optical properties relative to the lowest and highest reduced albedos, together with a case referred to typical optical properties,

i.e., $(\mu_a, \mu_s') = (0.01, 1)\ \text{mm}^{-1}$. In section "Comparison of fluence rate pathlengths in presence of a highly absorbing thin layer" we present the results for the medium with a thin highly absorbing layer. Finally, in section "Calculations of reflectance perturbation due to a strong localized absorption change" we present the results of perturbation of detected intensity caused by a large range of the absorption contrast between region of interest and background medium.

## Comparison of MC and diffusion theory results for the calculation of reflectance pathlengths

In Fig. 2 we show the comparison of $\langle l_i \rangle_{R_MC}$ obtained with the FORTRAN MC and MCX for the case of the cube of side 6 mm (Fig. 1). The calculations were run for $(\mu_a, \mu_s') = (0.02, 0.5)\ \text{mm}^{-1}$ (lowest reduced albedo). The results obtained with MCX are shown together with their errors obtained by running three independent simulations. In the same plots $\langle l_i \rangle_R$ and $\langle l_i \rangle_\phi$ obtained with DT (Eqs. 28, 29, respectively) are also shown. For the case of $\langle l_i \rangle_\phi$ the fluence rate was calculated at $z = 0$ (i.e., the detector was at $\mathbf{r} = \mathbf{r}_b = (\rho, 0{,}0)$). The results obtained with the two MC codes match within statistical error, which is shown only for the MCX code. Even with this choice of the optical properties, we can see a good agreement between the two MC results and with DT, especially with $\langle l_i \rangle_R$, as is expected. The maximum discrepancy between the two types of mean pathlengths according to DT is about 70% at the source-detector separation $\rho = 15$ mm and depth of the region of interest $z = 12$ mm, and becomes smaller at $\rho = 25$ mm and $\rho = 35$ mm. In Fig. 3 we show the same comparison for the highest reduced albedo: $(\mu_a, \mu_s') = (0.005, 1.5)\ \text{mm}^{-1}$.

There is an excellent agreement between the two MC codes and between them and DT, especially for $\langle l_i \rangle_R$. The discrepancy between the two types of mean pathlengths are less than about 10% for all cases considered. For other values of the optical properties, we found an excellent agreement between MC codes, while the agreement between the two types of pathlength depended mostly on $\mu_s'$ and little on the values of $\mu_a$. These tests show the consistency of the independent methods of calculation.

## Comparison of MCX and diffusion theory results for the calculation of fluence rate and reflectance pathlengths

In Fig. 4 we show the comparison of fluence rate partial pathlengths (Eq. 29) calculated with both MC and DT for the optical properties: $(\mu_a, \mu_s') = (0.02, 0.5)\ \text{mm}^{-1}$. In this case the region of interest was a cube of 1 mm side (Fig. 1) and was scanned at the depths $z = 6.5, 12.5, 20.5$ mm (top, middle and bottom row, respectively).

For the calculation of $\langle l_i \rangle_\phi$ with MCX, the direct simulations were carried out for a pencil beam at (0, 0, 0). The adjoint simulations were carried out in two different ways: (1) for the case of an isotropic point source at $(\rho, 0, s/2)$ ($\langle l_i \rangle_{\phi_MCX(z=\frac{s}{2})}$); (2) for a pencil beam at $(\rho, 0{,}0)$ ($\langle l_i \rangle_{\phi_MCX(z=1/\mu_s')}$), respectively. For the denominator of Eq. (29), $\mathbf{r}$ was chosen either as $\mathbf{r} = (\rho, 0, s/2)$ ($s = 1$ mm is the voxel size) for case 1), or $\mathbf{r} = (\rho, 0{,}1/\mu_s')$ for case 2). The reflectance partial pathlength calculated with MCX ($\langle l_i \rangle_{R_MCX}$), using detectors' areas specified in section "Monte Carlo simulations", are also reported. MCX results are plotted with their standard deviations obtained with three independent simulations.

We note that for $\langle l_i \rangle_\phi$ the results are more sensitive on the details of the adjoint calculation and the normalization factor, especially for this case (lowest reduced albedo). All the different methods have different biases with respect to $\langle l_i \rangle_{R_MC}$, which is the real target for reflectance calculations. We note a discrepancy among the methods also at the depth of $z = 20.5$ mm. One clear advantage of using the adjoint method with the MC method is the improvement of the statistical error on $\langle l_i \rangle_\phi$ with respect to the conventional method for the calculation of $\langle l_i \rangle_{R_MC}$. This is visible more clearly at $z = 20.5$ mm. The comparisons of partial pathlengths for the optical properties $(\mu_a, \mu_s') = (0.01, 1)\ \text{mm}^{-1}$ and $(\mu_a, \mu_s') = (0.005, 1.5)\ \text{mm}^{-1}$ are shown in Figs. 5 and 6, respectively. From these figures we can see that the difference between DT and MC calculations becomes almost negligible. This is also true for the two types of mean pathlengths regardless of the details of the calculations. In Figs. 5 and 6 the discrepancies between $\langle l_i \rangle_\phi$ and $\langle l_i \rangle_{R_MC}$ at the source-detector separation of 35 mm for locations close to the detector are an effect of the large detectors used for the calculation of $\langle l_i \rangle_{R_MC}$ : the detector's radius is 6.2 mm in Fig. 5, and 4.3 mm in Fig. 6. The discrepancies disappear once we choose a detector of smaller size (see Supplementary Information S5). We finally note that the calculation of $\langle l_i \rangle_\phi$ with DT and $\mathbf{r} = (\rho, 0, s/2)$ represents a slight overestimation of the same type of calculation for $\mathbf{r} = \mathbf{r}_b = (\rho, 0, 0)$ which amounts to about 5–6% at the shortest source-detector separation for $(\mu_a, \mu_s') = (0.02, 0.5)\ \text{mm}^{-1}$. The overestimation becomes 1–2% in all the other cases. One may infer that a similar consideration would apply to MC calculations.

## Comparison of fluence rate pathlengths in presence of a highly absorbing thin layer

Last, in Fig. 7, we want to explore how Rytov approximation behaves for a medium containing a highly absorbing layer (Fig. 1). By studying this case we can get a sense about the correctness of this approximation for the calculation of Jacobians, in the presence of discrete strong absorbers like blood vessels. We show the comparison between $\langle l_i \rangle_{R_MC}$ and $\langle l_i \rangle_\phi$ for a medium with 1 mm thick layer at the depth of $z = 6.5$ mm . The optical properties of the bulk of the medium are $(\mu_{ab}, \mu_{sb}') = (0.01, 1)\ \text{mm}^{-1}$, while for the absorbing layer $\left(\mu_{a,mel}, \mu_{s,mel}'\right) = (2, 1)\ \text{mm}^{-1}$.

The absorption of the thin layer can be representative of melanin in the epidermis, but the location can be representative of a blood vessel. The source-detector separation is $\rho = 35$ mm and the area of the detector 1 $\text{mm}^2$. The region of interest (cube of 1 mm side) was scanned along the $x$ axis at a depth of z = 12.5 mm. We considered $\langle l_i \rangle_\Phi$ calculated in the same two ways as in Figs. 4, 5 and 6. As we can see, the three calculations show a good agreement to within statistical errors. These results give us confidence that the Rytov approximation can be applied for the calculation of absorption Jacobians also in presence of strong absorbers. However, we want to

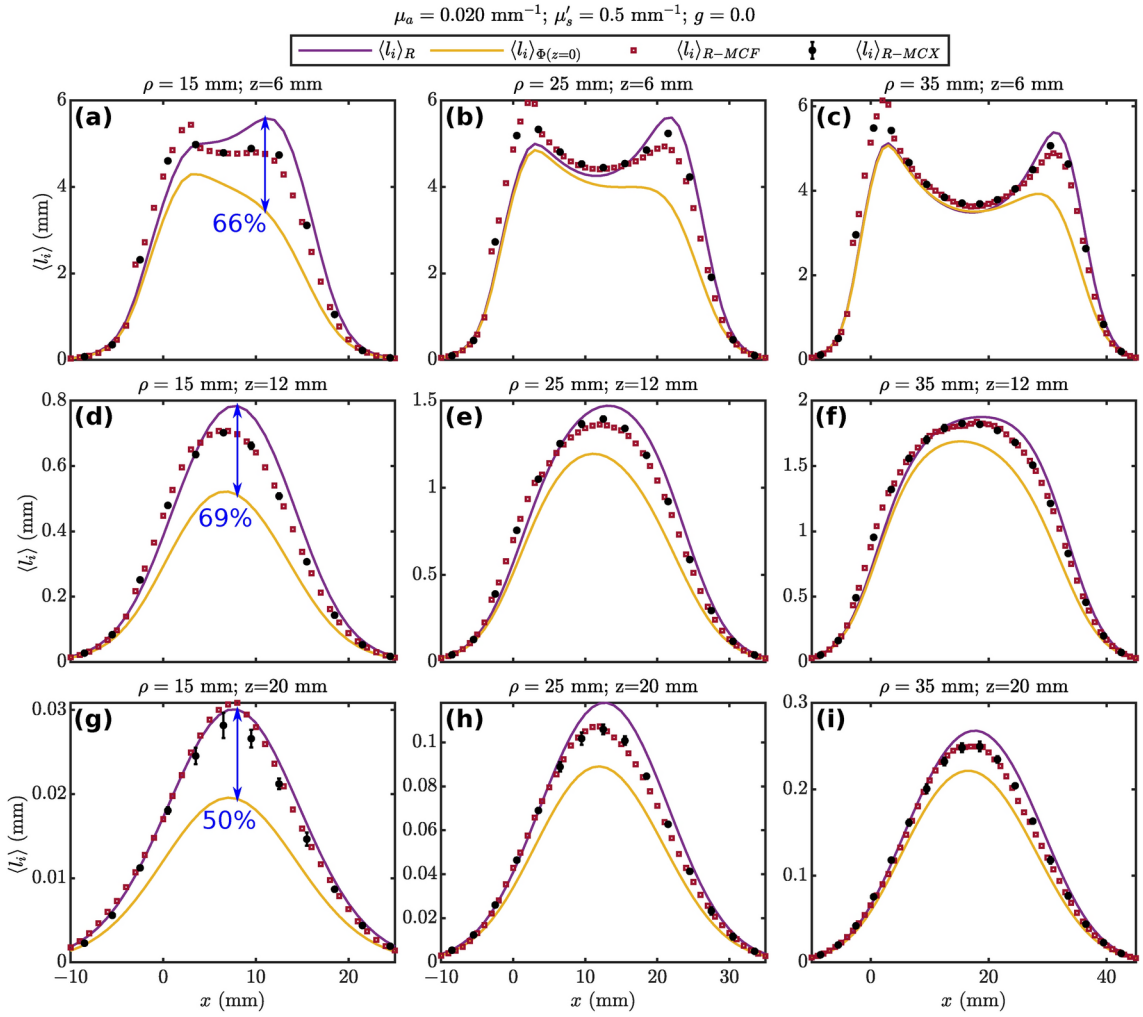


**Fig. 2**. Comparison of $\langle l_i \rangle_{R_MC}$ (Eq. 31) obtained with MCX ($\langle l_i \rangle_{R_MCX}$) and FORTRAN MC ($\langle l_i \rangle_{R_MCF}$) and with those obtained with DT (Eqs. 28, 29), $\langle l_i \rangle_R$ and $\langle l_i \rangle_{\phi(z=0)}$. The cube of side 6 mm (Fig. 1) was scanned along the $x$ axis at three different depths: $z = 6, 12, 20$ mm (top, middle and bottom row, respectively; $z$ is the center of the cube) and for the three detectors of Fig. 1 at the distance $\rho = 15, 25, 35$ mm (1st, 2nd, and 3rd column, respectively). The optical properties of the medium are: $(\mu_a, \mu_s') = (0.02, 0.5)$ mm$^{-1}$ (lowest reduced albedo). Double arrows indicating the discrepancy between $\langle l_i \rangle_R$ and $\langle l_i \rangle_{\phi(z=0)}$ (i.e., $\left(\langle l_i \rangle_R - \langle l_i \rangle_{\phi(z=0)}\right) / \langle l_i \rangle_{\phi(z=0)}$) are shown at the source-detector distance $\rho = 15$ (panels (a), (d) and (g)).

caution about possible problems when the thin absorbing layer is at the boundary (as a true melanin layer). To avoid these problems, we have proposed a calibration method[38].

These results are shown in Fig. 8, where we can see that the discrepancies between the two pathlengths are large, especially when we consider an adjoint simulation with a pencil beam at the detector's location and the normalization is carried out at $\mathbf{r} = (\rho, 0, 1/\mu_s')$ (orange symbols). We notice that the main difference between the correct Jacobian (black symbols) and the blue and orange symbols is an amplitude factor. This is mostly due to the rapid decrease of the fluence rate inside the melanin layer which causes a large overestimation of the denominator in Eq. (29) when we approximate the true normalization factor (i.e., the fluence rate at $z = 0$) with those used in the simulations. One solution could be to use a much smaller voxel size; however, the simulation will have to run for a longer time to have the same statistical significance. Besides, there might also be a small effect due to the highly absorbing layer, which close to the detector implies that photons travelling along certain directions are more likely to be detected. Another solution is to apply a calibration method. The calibration method we have proposed[38], imposes that the total mean pathlength calculated in the whole medium by using the Rytov approximation at each voxel coincides with the total mean pathlength $\langle L \rangle_{R_MC}$. In other words, the mean pathlength in a voxel "$i$" according to the Rytov approximation $\langle l_i \rangle_\phi = \frac{G_{\phi_0}(\mathbf{r}_0 \to \mathbf{r}_i') G_{\phi_0}(\mathbf{r}_i' \to \mathbf{r}_b)}{G_{\phi_0}(\mathbf{r}_0 \to \mathbf{r}_b)} dV$ is multiplied by a factor $\beta$ such that $\beta \sum_{i=1}^{N} \langle l_i \rangle_\phi = \langle L \rangle_{R_MC}$. This calibration is done for the two adjoint

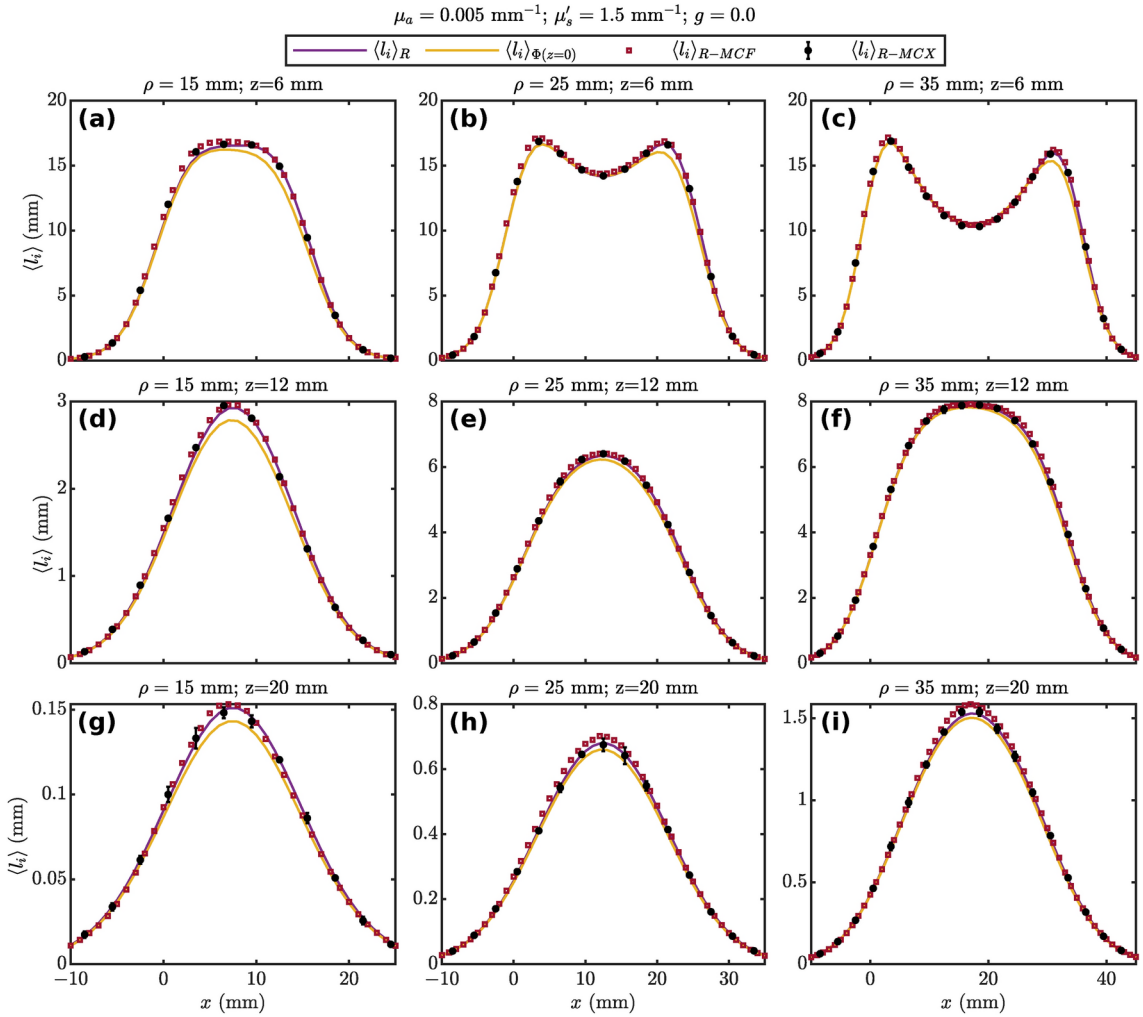


**Fig. 3**. As in Fig. 2 but for the optical properties $(\mu_a, \mu_s') = (0.005, 1.5)\ \text{mm}^{-1}$ (highest reduced albedo).

simulations discussed above, i.e., for the adjoint simulation with the isotropic source (for which $\beta = 1.76$) and the pencil beam (for which $\beta = 9.41$). The calibration method shows excellent comparison with $\langle l_i \rangle_{R_MC}$.

## Calculations of reflectance perturbation due to a strong localized absorption change

In this section we show two comparisons between calculations of reflectance change with respect to a baseline value (i.e., $\frac{\Delta R}{R_0}$) for a wide range of absorption change (i.e., $\Delta\mu_a$) between the region of interest and the background medium. The purpose is to show the performance of the Rytov approximation for reflectance (Eq. 22) with respect to the Born approximation and higher order Born series up to the fourth order. For higher order Born series we used a heuristic method proposed previously[21] (section "Diffusion theory calculations").

For each source-detector pair of Fig. 1 we chose a single cubic defect of side 6 mm placed at the depth of $z = 12$ mm and half-way between the source and the detector. The exact coordinates of each defect are provided in the title of Fig. 9. The baseline optical properties of the diffusive medium were: $(\mu_a, \mu_s') = (0.005, 1.5)\ \text{mm}^{-1}$. MC simulations were run for $g = 0$. The change of the absorption coefficient between the defect and the background medium spanned the range $\Delta\mu_a \in (0, 0.04)\ \text{mm}^{-1}$ with increments of $0.001\ \text{mm}^{-1}$. The reason to target large absorption change is to describe perturbations due to the presence of blood vessels. Figure 9 shows $\frac{\Delta R}{R_0}$ calculated with the first four order of the Born series (the 1st one is the Born approximation discussed in section "Born and Rytov approximations and their physical meaning"), with the reflectance under the Rytov approximation (Eq. 22), and with the FORTRAN MC code. As expected, the results obtained with the Rytov approximation have a smaller discrepancy with respect to MC results than 1st order Born series. However, the higher order Born series outperforms the Rytov approximation (as expected). In Fig. 10 we show another example for different optical properties of the background medium $(\mu_a, \mu_s') = (0.02, 1.5)\ \text{mm}^{-1}$ and for values of $\Delta\mu_a \in (-0.019, 0.04)\ \text{mm}^{-1}$.

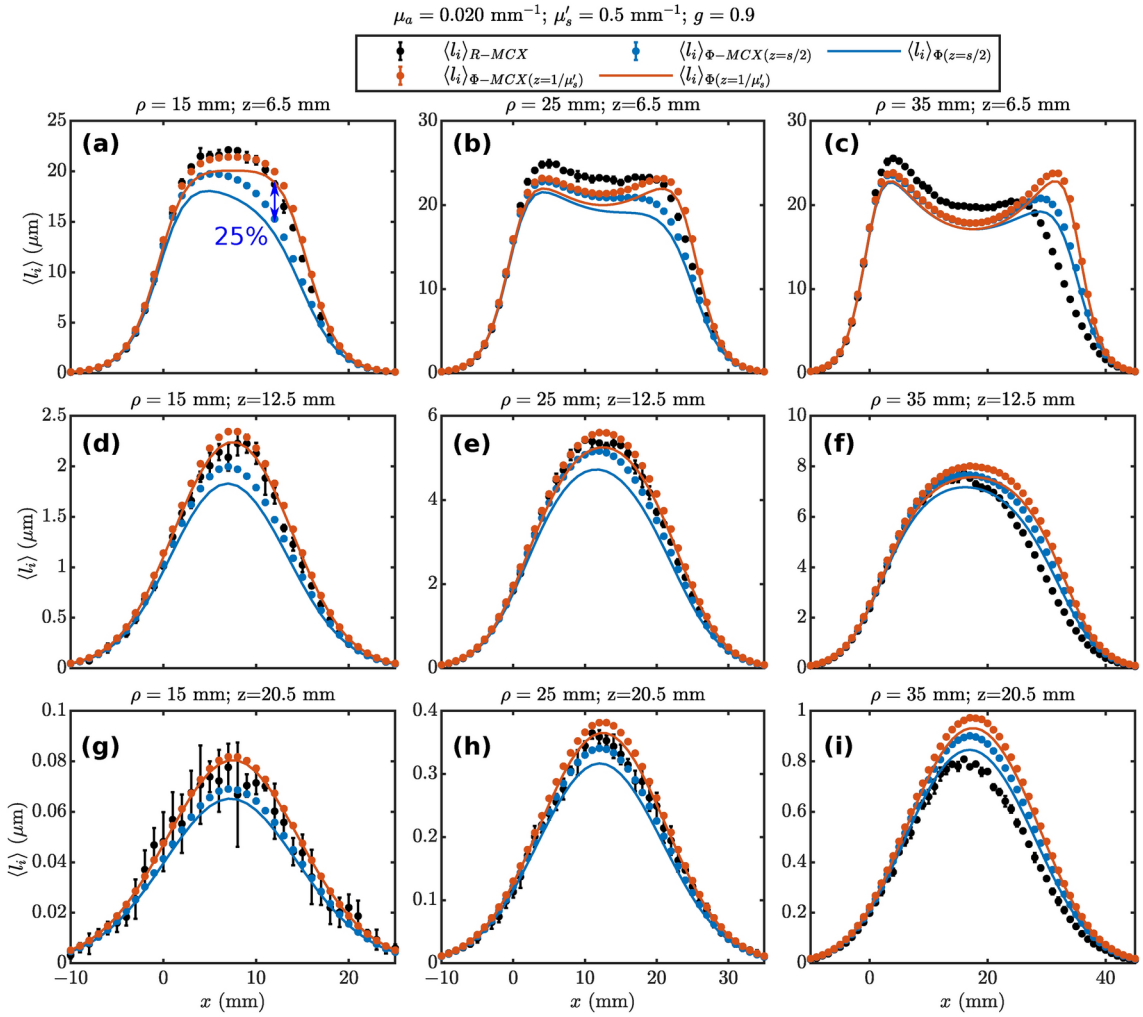


**Fig. 4**. Comparison of $\langle l_i \rangle_\phi$ obtained with MCX and DT according to Eq. (29), and $\langle l_i \rangle_{R_MC}$. A cube of side 1 mm was scanned along the $x$ axis at three different depths: $z = 6.5, 12.5, 20.5$ mm (top, middle and bottom row, respectively) and for the three detectors of Fig. 1 at the distance $\rho = 15, 25, 35$ mm (1$^{st}$, 2$^{nd}$, and 3$^{rd}$ column, respectively). The symbols refer to MCX results for: $\langle l_i \rangle_{R_MC}$ ($\langle l_i \rangle_{R_MCX}$), $\langle l_i \rangle_\phi$ obtained with an isotropic point source at $\mathbf{r} = (\rho, 0, s/2)$ ($\langle l_i \rangle_{\phi_MCX(z=\frac{s}{2})}$), and for $\langle l_i \rangle_\phi$ obtained with a pencil beam at $= (\rho, 0, 0)$ ($\langle l_i \rangle_{\phi_MCX(z=1/\mu_s')}$) for the adjoint calculations. The lines refer to DT calculations of $\langle l_i \rangle_\phi$ with $\mathbf{r} = (\rho, 0, s/2)$ ($\langle l_i \rangle_{\phi(z=\frac{s}{2})}$), and with $\mathbf{r} = (\rho, 0, 1/\mu_s')$ ($\langle l_i \rangle_{\phi(z=1/\mu_s')}$). The optical properties are: $(\mu_a, \mu_s') = (0.02, 0.5)$ mm$^{-1}$. A double arrow indicating the maximum discrepancy between $\langle l_i \rangle_{R_MCX}$ and $\langle l_i \rangle_{\phi_MCX(z=\frac{s}{2})}$ (i.e., $\left( \langle l_i \rangle_{R_MCX} - \langle l_i \rangle_{\phi_MCX(z=\frac{s}{2})} \right) / \langle l_i \rangle_{\phi_MCX(z=\frac{s}{2})}$) is shown in panel (a).

These two results are not surprising since the Rytov approximation (unlike the Born approximation) depends on higher powers of $\Delta\mu_a$, but the coefficient of each power is $\langle l_i \rangle_\phi^k$ and not the correct higher order moment $\langle l_i^k \rangle_\phi$. One way to improve the Rytov approximation will be proposed in section "Conclusions and future work".

## Discussions

In this work we have revisited the current use of the Rytov approximation in diffuse optics. One of the main applications we focused on is the well-known use of the Rytov approximation for a fast computation of Jacobians with MC simulations. This method can be very time-efficient and effective to reduce statistical errors when compared to the traditional method of mean pathlength estimation, whenever diffusion conditions are verified. We have shown that the Rytov approximation has a natural physical meaning, once we reframe the photon transport process by using a statistical approach derived from the microscopic Beer–Lambert law. Given a region of interest where the Jacobian for absorption changes is calculated, and an observation point where the fluence rate is measured, the exponent in the Rytov approximation represents the mean partial pathlength travelled by photons inside the region of interest times the change of the absorption coefficient. We have called this partial pathlength, the fluence rate partial pathlength. We have argued that this partial pathlength and the partial

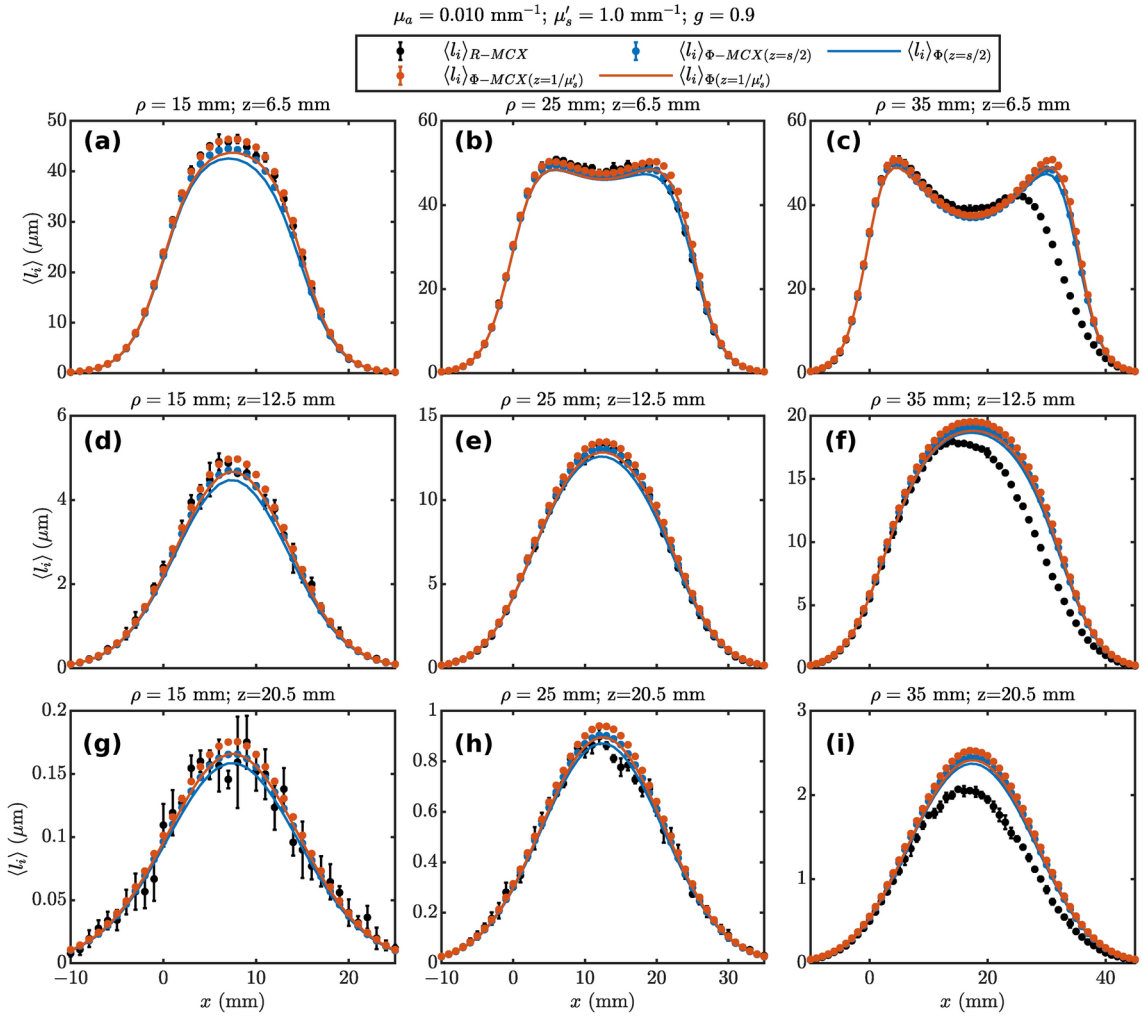


**Fig. 5**. As in Fig. 4 for typical values of the optical properties: $(\mu_a, \mu_s') = (0.01, 1)\ \text{mm}^{-1}$

pathlength defined for detected photons (named the reflectance partial pathlength) are distinct even when the observation point coincides with a detector point at the boundary. However, by physical arguments we can infer that these two pathlengths are similar in many situations of interest, even beyond DT. We can think of two correct methods to use MC simulations to calculate these two partial pathlengths. One way is to use a coupled forward-adjoint method[17] inspired by perturbation theory of RTE (Eqs. 25–27). This way can be efficient for variance reduction, but it may not be suitable for typical problems of DOT and NIRS, due to the high memory requirements. The other method, the conventional one, is to calculate the pathlength travelled by each detected photon inside a region of interest (see Supplementary Information S3). This method is suitable for NIRS and DOT applications and can be made more efficient by using the pseudorandom features of random number generators[19,37]. However, due to large memory requirements, even this method may not be suitable to calculate sensitivity maps for a fine voxelization of the medium. We stress that these are the only two methods for the calculation of the absorption Jacobian in a general situation under the validity of RTE. Whenever diffusion conditions are met, one can use the Rytov approximation together with the reciprocity theorem to speed up the computation of Jacobians[19]. However, we note that the notion of "meeting diffusion condition" is not a binary one, but it is true at different levels of approximation depending on the parameters of each case. This consideration prompted us to carry out more in-depth tests between the Jacobians obtained with the Rytov approximation (i.e., $\langle l_i \rangle_\phi$) and those obtained with reflectance measurements using both DT and MC (i.e., $\langle l_i \rangle_R$ and $\langle l_i \rangle_{R_MC}$, respectively). We have carried out comparisons for nine different combinations of the optical properties that span typical values found in NIRS and DOT. In a first series of tests (Figs. 2, 3), we have compared $\langle l_i \rangle_{R_MC}$ obtained with two independent MC codes and with DT (Eq. 28). In the same figures we also reported $\langle l_i \rangle_\phi$ based on DT (Eq. 29). The comparison of the two MC codes shows excellent agreement in all the cases studied. DT calculations have shown different levels of agreement with MC data, depending on the optical properties of the medium and the source-detector separation. For the case of $(\mu_a, \mu_s') = (0.02, 0.5)\ \text{mm}^{-1}$ both $\langle l_i \rangle_R$ and (especially) $\langle l_i \rangle_\phi$ show some discrepancy with the partial pathlength calculated by MC simulations (Fig. 2). For the case of $\langle l_i \rangle_\phi$, these discrepancies reach to about 70% at $\rho = 15$ mm, and $z = 12$ mm. We note that the discrepancies between $\langle l_i \rangle_\phi$ and $\langle l_i \rangle_R$ would not exist if one adopted PCBC. However, it is unlikely that

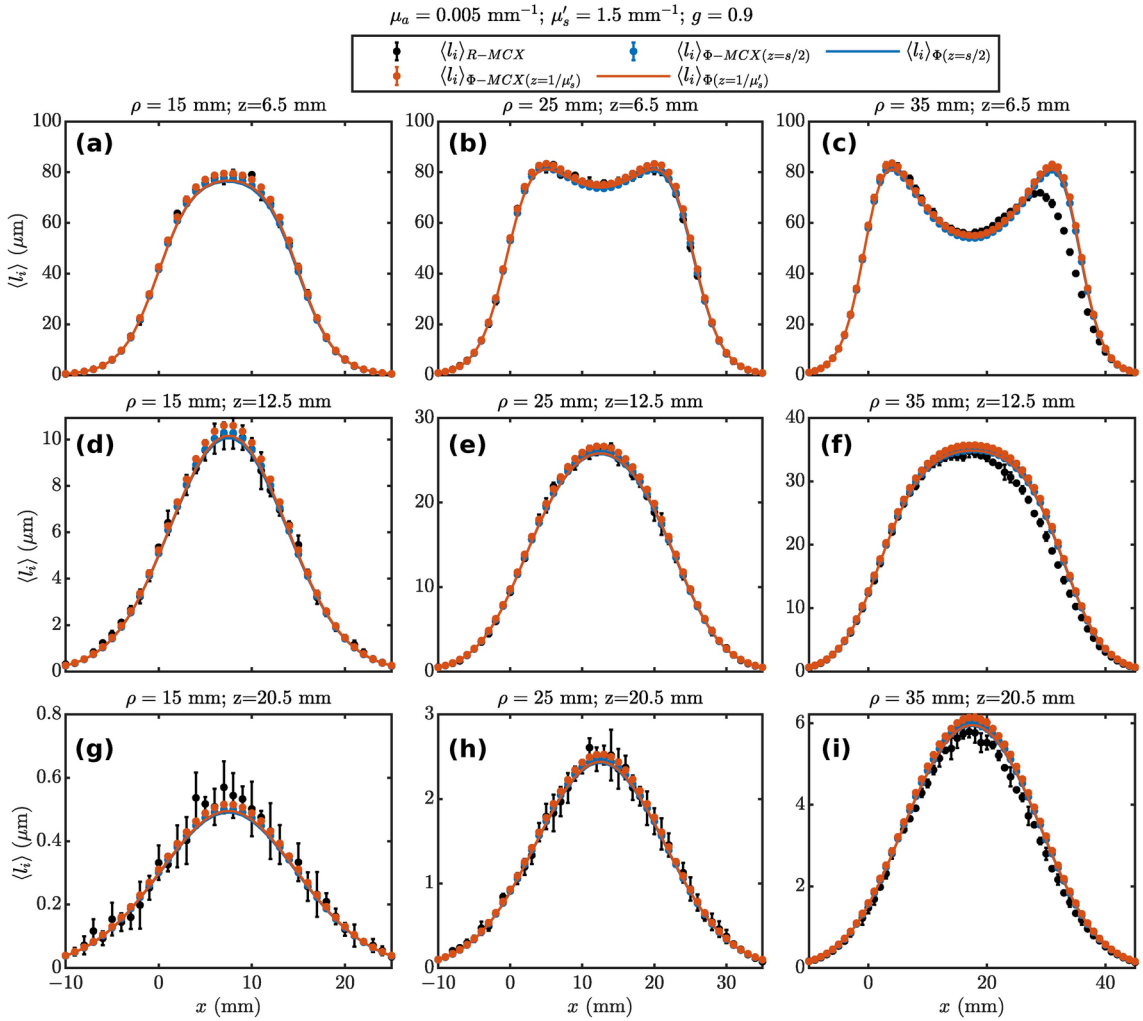


**Fig. 6**. As in Fig. 4 for values of the optical properties: $(\mu_a, \mu_s') = (0.005, 1.5)\ \text{mm}^{-1}$.

the results obtained with PCBC would be a better match with MC results. In fact, the literature has shown different results about the comparison of DE solutions based on EBC (like in this work) and PCBC, with MC results[39–41]. Therefore, we think that the most plausible explanation for these discrepancies is a combination of factors, including the relatively short source-detector separation, the choice of the optical properties (i.e., higher absorption and lower reduced scattering coefficients) and the approximate nature of any boundary condition for the DE. One should be aware of these factors if DT is used for the calculation of Jacobians. The more the diffusion conditions are fulfilled (i.e., larger source-detector separation and higher reduced scattering coefficient) the less discrepancies are found between MC and DT calculations, and between the two types of partial pathlengths (Fig. 3). These results are confirmed also in Figs. 4, 5, and 6, where we have used MCX for the calculation of $\langle l_i \rangle_\phi$. In this case, the shortcomings due to the approximate boundary conditions of DE are taken out of the picture. As a result, we can see a better agreement between $\langle l_i \rangle_{R_MC}$ and $\langle l_i \rangle_\phi$. The adjoint MC simulations for the calculation of $\langle l_i \rangle_\phi$ were run in two different ways: (a) by considering an isotropic point source at $\mathbf{r} = (\rho, 0, s/2)$; (b) by considering a pencil beam at $\mathbf{r}_b = (\rho, 0, 0)$. The normalization factor was chosen as $G_{\phi_0}(\mathbf{r}_0 \to \mathbf{r})$ for case a) and $G_{\phi_0}(\mathbf{r}_0 \to \mathbf{r}_1)$ for case b) where $\mathbf{r}_1 = (\rho, 0, 1/\mu'_s)$. In the same figures we have also reported the corresponding DT calculations of $\langle l_i \rangle_\phi$ (Eq. 29) and $\langle l_i \rangle_{R_MC}$ calculated with MCX. For the lowest value of the reduced albedo (Fig. 4), method (a) shows discrepancy up to ~ 25% with respect to $\langle l_i \rangle_{R_MC}$ at a depth of 6.5 mm and for $\rho = 15$ mm; method (b) yields the best comparison with $\langle l_i \rangle_{R_MC}$. As diffusion conditions are more and more satisfied (Figs. 5, 6), both methods are substantially equivalent and $\langle l_i \rangle_\phi \approx \langle l_i \rangle_R$. Therefore, these results suggest that method b) is a better choice for a wider range of optical properties.

In this work we bring to the attention of the scientific community the fact that the correct adjoint simulation for the calculation of the Jacobians for reflectance measurements should use an appropriate adjoint source at the detector's site (section "Relationship between the correct forward-adjoint method and the present work"). This fact has been previously stated in some literature of DT[6] and MC[17]. In other words, the calculation of the detected reflectance due to an isotropic source at the voxel $\mathbf{r}'$ is equivalent to the calculation of the fluence rate at the same voxel due to an appropriate adjoint source located at the detector. We have described in detail the

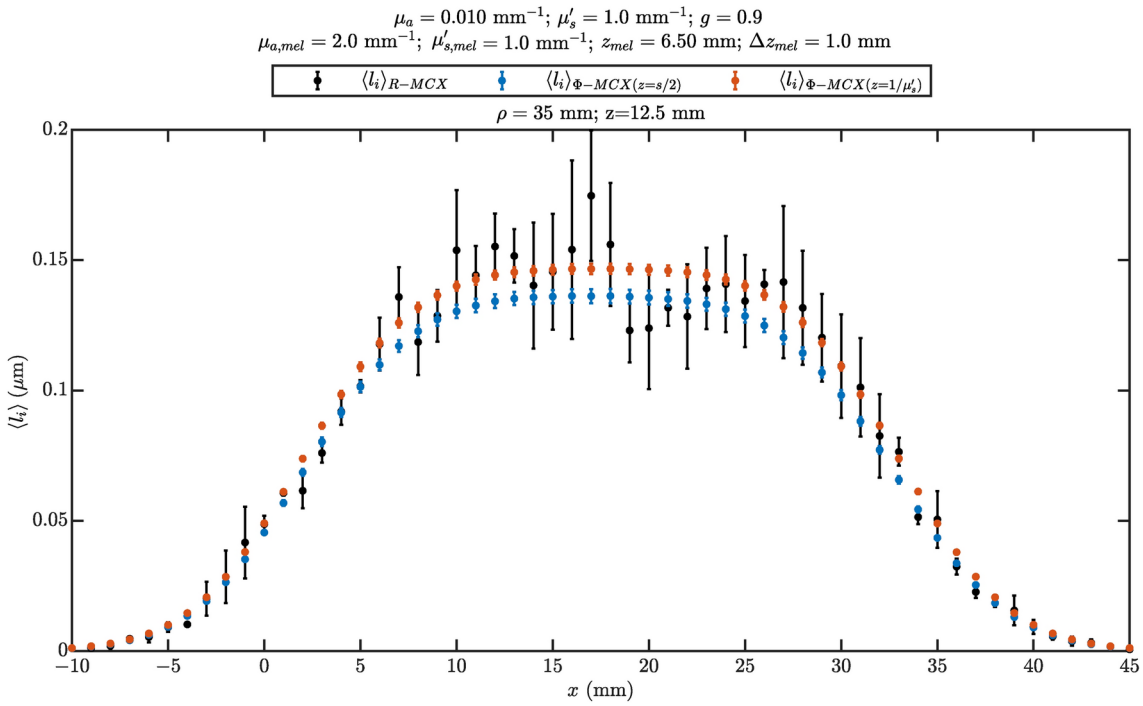


**Fig. 7**. Comparison of $\langle l_i \rangle_{R_MC}$($\langle l_i \rangle_{R_MCX}$) and $\langle l_i \rangle_{\phi}$($\langle l_i \rangle_{\phi_MCX(z=\frac{s}{2})}$, $\langle l_i \rangle_{\phi_MCX(z=1/\mu'_s)}$) obtained with MCX for a homogeneous medium containing a 1 mm thick highly absorbing layer with its center at the depth $z = 6.5$ mm (Fig. 1). The optical properties are: $(\mu_{ab}, \mu'_{sb}) = (0.01, 1)$ mm$^{-1}$ and $(\mu_{a,mel}, \mu'_{s,mel}) = (2, 1)$ mm$^{-1}$, for the bulk of the medium and for the thin layer, respectively. The source-detector separation is $\rho = 35$ mm and the area of the detector is 1 mm$^2$ (for the calculation of $\langle l_i \rangle_{R_MC}$). The region of interest (cube of 1 mm side) was scanned along the $x$ axis at a depth of $z = 12.5$ mm. The blue and orange symbols correspond to the adjoint simulations with isotropic source and the pencil beam, respectively.

properties of this adjoint source in section "Relationship between the correct forward-adjoint method and the present work". This would allow the calculation of $\langle l_i \rangle_R$ by using MC-calculated fluence rate and reflectance. To the best of our knowledge this feature is not currently implemented in MCX. Most probably this method could yield better results than the calculation of $\langle l_i \rangle_\phi$ with method b) above.

By using only MC simulations, we have also reported two comparisons between $\langle l_i \rangle_{R_MC}$ and $\langle l_i \rangle_\phi$ for a medium with a highly absorbing thin layer (having a thickness of 1 mm) embedded in it. The purpose of these examples was twofold: (a) We wanted to show that the Rytov approximation (when applied correctly) is a valid method for the calculation of Jacobians even in presence of a strong absorber. The optical properties of the thin layer were typical of melanin even when it was embedded at a depth of 6.5 mm (Fig. 7); (b) we wanted also to point out some "dangers" of the Rytov approximation when it is not applied correctly (Fig. 8). The example of Fig. 8 is particularly useful, given the widespread use of MCX for pulse oximetry simulations, where one of the current topics is the study of the effect of the melanin layer. In this case, the presence of the melanin layer causes a strong gradient of the fluence rate close to the boundary, and one would have to resort to a finer voxelization of the medium. To bypass this problem, in Fig. 8 we have also shown some results obtained with a novel calibration method that we have recently proposed[38]. This method yields an excellent agreement with $\langle l_i \rangle_{R_MC}$.

Finally, we have tested a novel formula for reflectance calculations under the Rytov approximation Eq. (22). We have calculated the change of reflectance caused by three localized absorption perturbations (a different one for each source-detector distance) for a wide range of the absorption contrast. As expected, the Rytov approximation performs better than the Born approximation but worse than the higher order Born series. Despite the Rytov approximation being nonlinearly dependent on $\Delta\mu_a$, it is based on the wrong assumption that $\langle l_i \rangle_\phi^k$ can substitute $\langle l_i^k \rangle_\phi$. We expect that higher order Rytov approximation[3] can show faster convergence than higher order Born series, as it is discussed in the next section.

## Conclusions and future work

In this work we have reviewed the use of the Rytov approximation in diffuse optics, especially the burgeoning application in MC simulations for the calculations of Jacobians. Under the validity of diffusion conditions, we have shown the natural physical meaning of the Rytov approximation, in terms of the fluence rate partial pathlength, which is directly related to the photon migration process. Based on this physical meaning, we have argued that for typical values of the optical properties in NIRS and DOT, the fluence rate pathlength is a close representation of the reflectance pathlength. In other words, in these situations the Rytov approximation can be

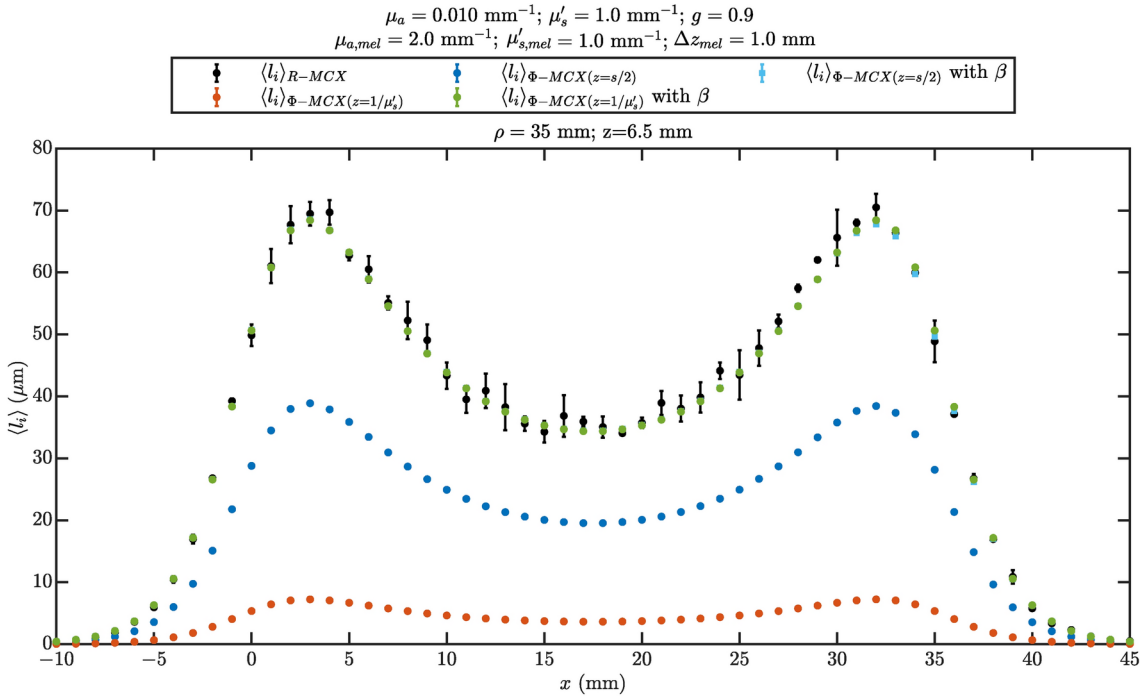


**Fig. 8**. Comparison of $\langle l_i \rangle_{R_MC}$ ($\langle l_i \rangle_{R_MCX}$) and $\langle l_i \rangle_{\phi}$ (other symbols) obtained with MCX for a medium with a 1 mm thick layer at the boundary with the outer medium (i.e., depth of the center of the layer is $z = 0.5$ mm). The optical properties, source-detector separation, area of the detector, and voxel size are as in Fig. 7. The region of interest (cube of 1 mm side) was scanned along the $x$ axis at a depth of $z = 6.5$ mm. The blue and orange symbols correspond to the adjoint simulations with isotropic source ($\langle l_i \rangle_{\phi_MCX(z=\frac{s}{2})}$) and the pencil beam ($\langle l_i \rangle_{\phi_MCX(z=1/\mu_s')}$), respectively. The cyan ($\langle l_i \rangle_{\phi_MCX(z=\frac{s}{2})}$ with $\beta$) and green ($\langle l_i \rangle_{\phi_MCX(z=1/\mu_s')}$ with $\beta$) symbols correspond to the adjoint simulations after applying the proposed calibration method (which identifies a factor $\beta$) to the blue and orange plots, respectively.

used as a good surrogate of $\langle l_i \rangle_{R_MC}$, especially if one uses a particular adjoint simulation with a pencil beam at the detector's site and normalization of the fluence rate calculated at the diffusion length ($1/\mu'_s$). One alternative way, which is more logical for reflectance measurement is to use an appropriate adjoint simulation (based on general properties of the reciprocity theorem) that directly targets this type of measurement. This method is known in the scientific literature[6,17] but not currently implemented in MCX.

In principle the method of mean pathlength estimation trough propagation of the photons and intersection with a region of interest is valid in general conditions without any approximation. Future work will be directed for finding strategies where this method can be used to provide detailed sensitivity maps of the absorption coefficient avoiding memory issues. We also plan to do more testing and to refine the calibration method proposed in Blaney et al.,[38]. One method can be to define several calibration factors, for example as many as some macroscopic regions of interest. For example, in a layered model of the finger one could define layer-specific calibration factors. Last, we plan to use the Rytov series together with the heuristic calculation of higher order moments for a faster convergence of perturbation calculations for large absorption contrasts. This method can be useful to speed up the convergence of forward problem calculations. In fact, the relationships between the different orders of the Born and Rytov series are well known[3]. These relationships can be reframed with the pathlength moments, which for the case of higher order Rytov series, leads to combinations of higher and lower moments and their powers. For example, while the second order normalized Born series leads to $\frac{1}{2}\langle l_i^2 \rangle \Delta\mu_{ai}^2$, the second order Rytov series is: $\psi_2 = \frac{1}{2}\left[\langle l_i^2 \rangle - \langle l_i \rangle^2\right] \Delta\mu_{ai}^2$. It is well possible that the higher order Rytov series will improve the convergence of perturbation calculations.

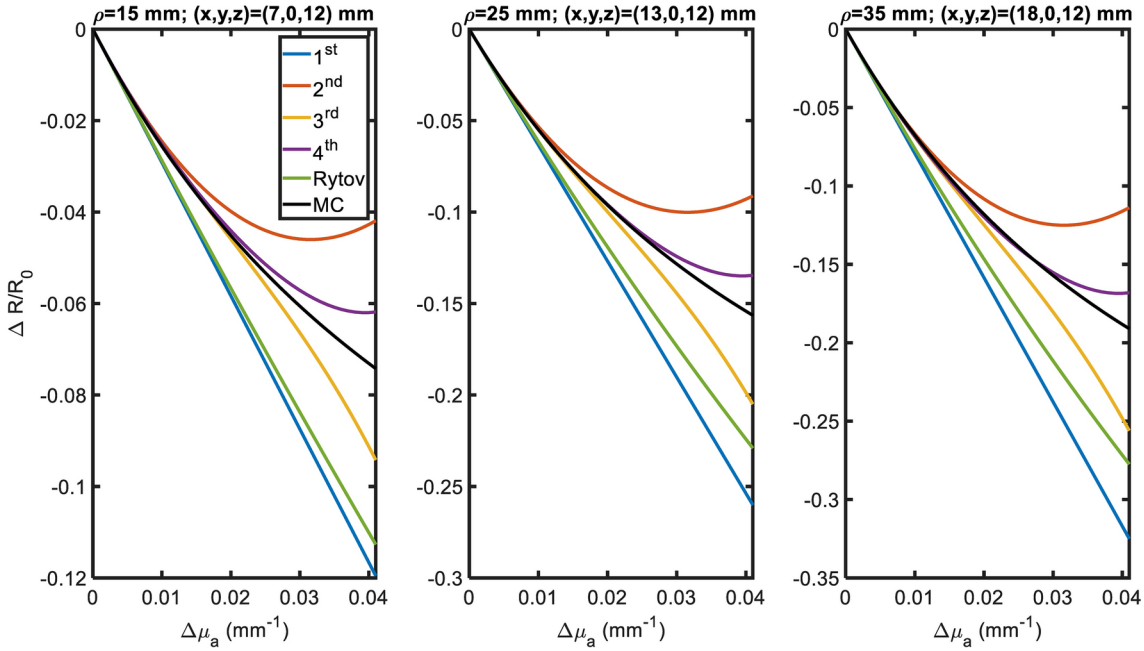


**Fig. 9**. Comparison of reflectance change $\frac{\Delta R}{R_0}$ calculated with the first four orders of Born series, with Rytov approximation and with the FORTRAN MC code at the source-detector separation of $\rho = 15$ mm (left panel), $\rho = 25$ mm (center panel) and $\rho = 35$ mm (right panel). For each source-detector pair the location of the defect (a cube of side 6 mm) is indicated in the title. The baseline properties of the medium are $(\mu_a, \mu_s') = (0.005, 1.5)$ mm$^{-1}$. The change of absorption coefficient between defect and background medium spans the range $\Delta\mu_a \in (0, 0.04)$ mm$^{-1}$ with increments of $0.001$ mm$^{-1}$.

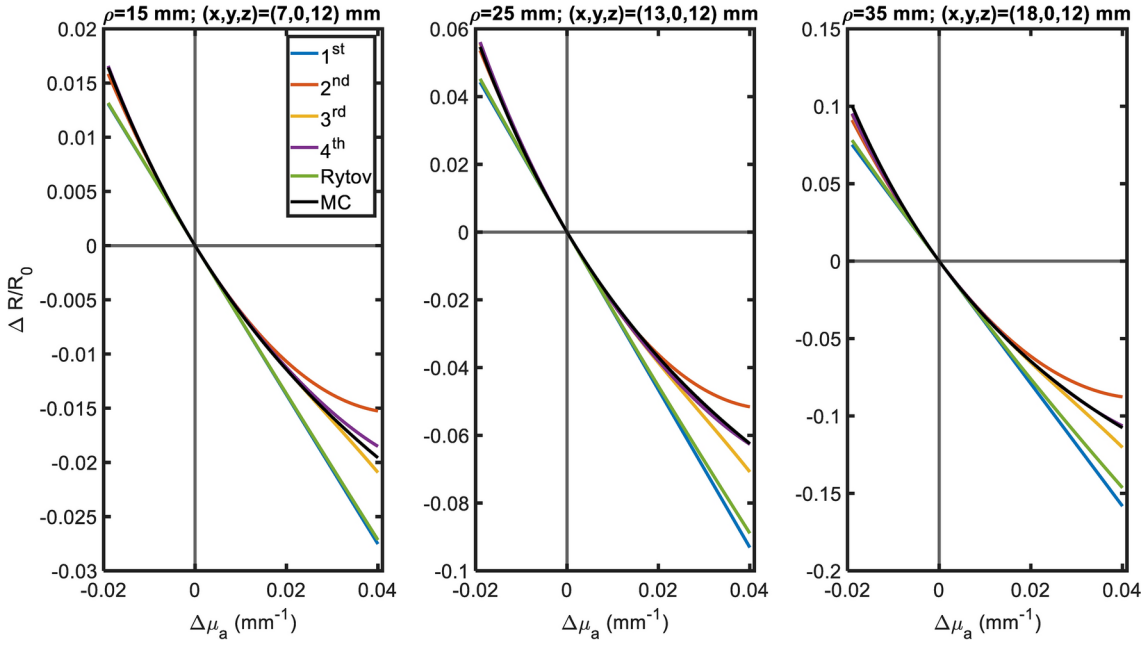


**Fig. 10**. As in Fig. 9 but for different values of the background medium optical properties: $(\mu_a, \mu_s') = (0.02, 1.5)$ mm$^{-1}$. The change of absorption coefficient was: $\Delta\mu_a \in (-0.019, 0.04)$ mm$^{-1}$

## Data availability

The datasets used and/or analysed during the current study available from the corresponding author on reasonable request.

Received: 30 August 2024; Accepted: 9 December 2024
Published online: 28 December 2024

## References

1. Cairns, B. & Wolf, E. Comparison of the Born and the Rytov approximations for scattering on quasi-homogeneous media. *Opt. Commun.* **74**, 284–289 (1990).
2. Kak, A. C. & Slaney, M. *Principles of Computerized Tomographic Imaging* (Society for Industrial and Applied Mathematics, 2001). https://doi.org/10.1137/1.9780898719277.
3. Potvin, G. General Rytov approximation. *JOSA A* **32**, 1848–1856 (2015).
4. Feng, B., Wu, R.-S. & Wang, H. Higher-order Rytov approximation for large-scale and strong perturbation media. *Commun. Comput. Phys.* **28**, 98–110 (2020).
5. Wu, R.-S. Wave propagation, scattering and imaging using dual-domain one-way and one-return propagators. *Pure Appl. Geophys.* **160**, 509–539 (2003).
6. Arridge, S. R. Optical tomography in medical imaging. *Inverse Probl.* **15**, R41 (1999).
7. Durduran, T., Choe, R., Baker, W. B. & Yodh, A. G. Diffuse optics for tissue monitoring and tomography. *Rep. Prog. Phys.* **73**, 076701 (2010).
8. O'Leary, M. *Imaging with Diffuse Photon Density Waves* (University of Pennsylvania, 1996).
9. Boas, D. A., Culver, J. P., Stott, J. J. & Dunn, A. K. Three dimensional Monte Carlo code for photon migration through complex heterogeneous media including the adult human head. *Opt. Express* **10**, 159–170 (2002).
10. Ntziachristos, V. & Weissleder, R. Experimental three-dimensional fluorescence reconstruction of diffuse media by use of a normalized Born approximation. *Opt. Lett.* **26**, 893–895 (2001).
11. Pyka, T., Schulz, R., Ale, A. & Ntziachristos, V. Revisiting the normalized Born approximation: Effects of scattering. *Opt. Lett.* **36**, 4329–4331 (2011).
12. Fang, Q. & Boas, D. A. Monte Carlo simulation of photon migration in 3D turbid media accelerated by graphics processing units. *Opt. Express* **17**, 20178–20190 (2009).
13. Ren, N. et al. GPU-based Monte Carlo simulation for light propagation in complex heterogeneous tissues. *Opt. Express* **18**, 6811–6823 (2010).
14. Alerstam, E., Svensson, T. & Andersson-Engels, S. Parallel computing with graphics processing units for high-speed Monte Carlo simulation of photon migration. *J. Biomed. Opt.* **13**, 060504 (2008).
15. Martelli, F., Binzoni, T., Del Bianco, S., Liemert, A. & Kienle, A. *Light Propagation through Biological Tissue and Other Diffusive Media: Theory, Solutions, and Validation* 2nd edn. (SPIE, 2022).
16. Yi, X. *et al.* Towards diffuse optical tomography of arbitrarily heterogeneous turbid medium using GPU-accelerated Monte-Carlo forward calculation. In *Multimodal Biomedical Imaging VIII* vol. 8574 108–117 (SPIE, 2013).
17. Hayakawa, C. K., Spanier, J. & Venugopalan, V. Coupled forward-adjoint Monte Carlo simulations of radiative transport for the study of optical probe design in heterogeneous tissues. *SIAM J. Appl. Math.* **68**, 253–270 (2007).
18. Gardner, A. R., Hayakawa, C. K. & Venugopalan, V. Coupled forward-adjoint Monte Carlo simulation of spatial-angular light fields to determine optical sensitivity in turbid media. *J. Biomed. Opt.* **19**, 065003 (2014).
19. Yao, R., Intes, X. & Fang, Q. Direct approach to compute Jacobians for diffuse optical tomography using perturbation Monte Carlo-based photon "replay". *Biomed. Opt. Express* **9**, 4588–4603 (2018).
20. Yan, S., Yao, R., Intes, X. & Fang, Q. Accelerating Monte Carlo modeling of structured-light-based diffuse optical imaging via "photon sharing". *Opt. Lett.* **45**, 2842–2845 (2020).
21. Sassaroli, A., Martelli, F. & Fantini, S. Perturbation theory for the diffusion equation by use of the moments of the generalized temporal point-spread function. I. Theory. *JOSA A* **23**, 2105–2118 (2006).
22. Serov, I. V., John, T. M. & Hoogenboom, J. E. A new effective Monte Carlo Midway coupling method in MCNP applied to a well logging problem. *Appl. Radiat. Isot.* **49**, 1737–1744 (1998).
23. White, B. R. & Culver, J. P. Quantitative evaluation of high-density diffuse optical tomography: In vivo resolution and mapping performance. *J. Biomed. Opt.* **15**, 026006 (2010).
24. Culver, J. P. et al. Three-dimensional diffuse optical tomography in the parallel plane transmission geometry: Evaluation of a hybrid frequency domain/continuous wave clinical system for breast imaging. *Med. Phys.* **30**, 235–247 (2003).
25. Wheelock, M. D., Culver, J. P. & Eggebrecht, A. T. High-density diffuse optical tomography for imaging human brain function. *Rev. Sci. Instrum.* **90**, 051101 (2019).
26. Fan, W., Dehghani, H. & Eggebrecht, A. T. Investigation of effect of modulation frequency on high-density diffuse optical tomography image quality. *Neurophotonics* **8**, 045002 (2021).
27. Tsuchiya, Y. Photon path distribution and optical responses of turbid media: Theoretical analysis based on the microscopic Beer–Lambert law. *Phys. Med. Biol.* **46**, 2067 (2001).
28. Hiraoka, M. et al. A Monte Carlo investigation of optical pathlength in inhomogeneous tissue and its application to near-infrared spectroscopy. *Phys. Med. Biol.* **38**, 1859 (1993).
29. Box, M. A., Keevers, M. & McKellar, B. H. J. On the perturbation series for radiative effects. *J. Quant. Spectrosc. Radiat. Transf.* **39**, 219–223 (1988).
30. Markel, V. A. & Schotland, J. C. On the convergence of the Born series in optical tomography with diffuse light. *Inverse Probl.* **23**, 1445 (2007).
31. Arfken, G. B. & Weber, H. J. *Mathematical Methods for Physicists* (Academic Press, 1995).
32. Duderstadt, J. J. & Martin, W. R. *Transport Theory* (1979).
33. Jha, A. K. et al. Simulating photon-transport in uniform media using the radiative transport equation: A study using the Neumann-series approach. *JOSA A* **29**, 1741–1757 (2012).
34. Case, K. M. & Zweifel, P. F. *Linear Transport Theory* (Addison-Wesley Publishing Company, 1967).
35. Aronson, R. Radiative transfer implies a modified reciprocity relation. *JOSA A* **14**, 486–490 (1997).
36. Sassaroli, A., Blaney, G. & Fantini, S. Novel data types for frequency-domain diffuse optical spectroscopy and imaging of tissues: Characterization of sensitivity and contrast-to-noise ratio for absorption perturbations. *Biomed. Opt. Express* **14**, 2091–2116 (2023).
37. Sassaroli, A. Fast perturbation Monte Carlo method for photon migration in heterogeneous turbid media. *Opt. Lett.* **36**, 2095–2097 (2011).
38. Blaney, G., Frias, J., Tavakoli, F., Sassaroli, A. & Fantini, S. Dual-ratio approach to pulse oximetry and the effect of skin tone. Preprint at https://doi.org/10.48550/arXiv.2405.15782 (2024).
39. Haskell, R. C. et al. Boundary conditions for the diffusion equation in radiative transfer. *JOSA A* **11**, 2727–2741 (1994).

40. Hielscher, A. H., Jacques, S. L., Wang, L. & Tittel, F. K. The influence of boundary conditions on the accuracy of diffusion theory in time-resolved reflectance spectroscopy of biological tissues. *Phys. Med. Biol.* **40**, 1957 (1995).
41. Kienle, A. & Patterson, M. S. Improved solutions of the steady-state and the time-resolved diffusion equations for reflectance from a semi-infinite turbid medium. *JOSA A* **14**, 246–254 (1997).

## Acknowledgements

This work is supported by the National Institutes of Health (NIH) award R01-EB029414. G.B. would also like to acknowledge support from NIH award K12-GM133314. F.M. acknowledges the European Union's—Next-GenerationEU, National Recovery and Resilience Plan, MNESYS, PE0000006 (DN. 1553 11.10.2022) and PRIN 2022, DIRS: 2022EB4B7E. The content is solely the authors' responsibility and does not necessarily represent the official views of the awarding institutions. The authors wish to acknowledge useful communications with Qianqian Fang. The authors wish also to acknowledge illuminating exchange with Carole Hayakawa about the coupled forward-adjoint method, and for reading the theory section of the manuscript.

## Author contributions

Conceptualization, A.S., G.B., F.M., and S.F.; methodology, A.S., G.B. and F.M.; software, G.B. and A.S.; data analysis, G.B. and A.S.; writing—original draft preparation, A.S.; writing—review and editing, A.S., G.B., F.M., and S.F.

## Declarations

## Competing interests

The authors declare no competing interests.

## Additional information

**Supplementary Information** The online version contains supplementary material available at https://doi.org/10.1038/s41598-024-82682-3.

**Correspondence** and requests for materials should be addressed to A.S.

**Reprints and permissions information** is available at www.nature.com/reprints.

**Publisher's note** Springer Nature remains neutral with regard to jurisdictional claims in published maps and institutional affiliations.

**Open Access** This article is licensed under a Creative Commons Attribution-NonCommercial-NoDerivatives 4.0 International License, which permits any non-commercial use, sharing, distribution and reproduction in any medium or format, as long as you give appropriate credit to the original author(s) and the source, provide a link to the Creative Commons licence, and indicate if you modified the licensed material. You do not have permission under this licence to share adapted material derived from this article or parts of it. The images or other third party material in this article are included in the article's Creative Commons licence, unless indicated otherwise in a credit line to the material. If material is not included in the article's Creative Commons licence and your intended use is not permitted by statutory regulation or exceeds the permitted use, you will need to obtain permission directly from the copyright holder. To view a copy of this licence, visit http://creativecommons.org/licenses/by-nc-nd/4.0/.

© The Author(s) 2024